Coversheet

Title: Automated landslide detection in SAR wrapped interferograms using a geomorphology-constrained YOLO CNN

Authors and Affiliations:

- Alessandro C. Mondini (1) - alessandro.mondini@ge.imati.cnr.it
- Alessandro Simoni (2) - [alessandro.simoni@unibo.it]
- Fabio Bovenga (3) - [fabio.bovenga@cnr.it]
- Alessandro Mercurio (2) - [alessandro.mercurio@unibo.it]
- Cristina Reyes-Carmona (4) – [cristina.reyescarmona@unimib.it]
- Boyun Yu (5) - [yu-boyun124@g.ecc.u-tokyo.ac.jp]
- Federico Agliardi (4) - [federico.agliardi@unimib.it]

(1) National Research Council CNR – IMATI, Genova, 16149, Italy

(2) Department of Biological, Geological, and Environmental Sciences, University of Bologna, Bologna, 40126, Italy

(3) National Research Council CNR – IREA, Bari, 70126, Italy

(4) Department of Earth and Environmental Sciences, University of Milano-Bicocca, Milano, 20126, Italy

(5) Graduate School of Frontier Sciences, The University of Tokyo. 5-1-5, Kashiwa-no-ha, Kashiwa City, Chiba, 277-8561, Japan

Corresponding Author: Alessandro C. Mondini (alessandro.mondini@ge.imati.cnr.it)

Declaration of Peer Review Status: This is a non-peer-reviewed preprint submitted to EarthArXiv.

Automated landslide detection in SAR wrapped interferograms using a geomorphology-constrained YOLO CNN

Alessandro C. Mondini[1], Alessandro Simoni[2], Fabio Bovenga[3], Alessandro Mercurio[2], Cristina Reyes-Carmona[4], Yu Boyun [5], Federico Agliardi[4]

[1] National Research Council CNR – IMATI, Genova, 16149, Italy
[2] Department of Biological, Geological, and Environmental Sciences, University of Bologna, Bologna, 40126, Italy
[3] National Research Council CNR – IREA, Bari, 70126, Italy
[4] Department of Earth and Environmental Sciences, University of Milano-Bicocca, Milano, 20126, Italy
[5] Graduate School of Frontier Sciences, The University of Tokyo. 5-1-5, Kashiwa-no-ha, Kashiwa City, Chiba, 277-8561, Japan

Correspondence to: Alessandro C.Mondini (alessandro.mondini@ge.imati.cnr.it)

Abstract

Slow-moving landslides pose significant hazards in mountain environments, requiring improved detection and monitoring capabilities. Traditional mapping is accurate but time-consuming, while multitemporal InSAR approaches are limited by data complexity and velocity constraints. Wrapped dual-pass DInSAR interferograms offer an alternative by preserving deformation signals without phase unwrapping, enabling detection across a wide range of movement rates.

We present a deep learning framework for the automated detection and classification of active slow landslides in Sentinel-1 wrapped SAR interferograms. The model uses a YOLO convolutional neural network ingesting wrapped phase, an InSAR reliability index, and a terrain morphometric attribute layer. We trained, validated, and tested the network on 2243 labelled DInSAR wrapped phase signals from expert geomorphological interpretation over a 1200 km² sector of the Northern Apennines (Italy), using interferograms from ascending and descending orbits generated with multiple temporal baselines between 6 and 30 days.

The network outputs bounding boxes with movement classification, achieving a mean Average Precision of 0.88 and an F1 score of 0.75. It successfully identifies deformation signals across multiple spatial scales, also in interferograms with low signal-to-noise ratio. Our results demonstrate the potential of wrapped DInSAR data combined with deep learning for efficient regional-scale landslide detection and inventory updating.

1 Introduction

Slow-moving landslides are widely recognized as primary drivers of slope dynamics, operating over timescales of months to centuries at rates ranging from millimetres to several metres per year. Their behaviour is highly variable, driven by diverse mechanisms that depend on the materials involved and the specific geomorphological setting (Hovius and Stark, 2006; Korup et al., 2010). Fluvial-dominated mountain ranges are typically characterized by rockslides and long-lived earthflows, typically characterized by very slow movements with fast episodic reactivations that have significant impacts on landscape morphology, stream network organization and flood hydrology (Mackey and Roering, 2011; Squarzoni et al., 2020).

The strong heterogeneity of involved geomaterials, topographic settings and triggering factors results in landslide processes spanning a wide range of volumes (10^3–10^8 m^3), displacement rates (from mm/yr to m/yr), spatial patterns and temporal trends of displacements, posing risks either through progressive structural damage caused by slow movements or through catastrophic collapse impacting lives and infrastructure (Froude and Petley, 2012; Handwerger et al., 2019; Agliardi et al., 2020; Lacroix et al., 2020; Agliardi and Crippa, 2022). Enhanced capabilities for rapid, wide-area detection, classification, and monitoring of mass movements are therefore essential to support land-use planning, protect life and property, and reduce disaster risk—particularly in mountain regions increasingly subjected to anthropogenic pressures under climate change.

Traditional regional-scale approaches for detecting and characterizing mass movement activity rely on manual geomorphological mapping supported by field observations and ground-based or spaceborne remote sensing data (Guzzetti et al., 2012). Among these, multi-spectral, radar and lidar imaging techniques have been increasingly used and developed since the early 2000s (Casagli et al., 2023). Although highly accurate and process-oriented, these methods are time-consuming and difficult to update over large areas.

Since its appearance (Fruneau et al., 1996), synthetic-aperture radar interferometry (InSAR) offered a breakthrough in the identification, characterization and monitoring study of mass movements. Automated processing exploits multiple interferograms to generate time series of ground displacement (Ferretti et al., 2002; Berardino et al., 2003), allowing the systematic analysis of large regions where displacement time-series can be retrieved for coherent scatterers (Raspini et al., 2019). However, the ability of InSAR techniques to capture landslide displacements strongly depend on several factors including radar band and geometry, slope topography and landcover, environmental disturbances (e.g. atmosphere, snow), and observed landslide displacement rate (Wasowski and Bovenga, 2014). These affect the radar detection threshold and InSAR coherence. Thus, InSAR applications to landslides must be carefully tailored to the specific processes and environments of interest, with the support of sound geological and geomorphological constraints.

Modern satellite missions like Sentinel-1 provide systematic acquisitions in space and time, high orbital precision and radar images with unprecedented resolutions. This allows obtaining multi-temporal InSAR products providing millimetre-scale deformation measurements and time series of long-term displacements useful for mass movement recognition (Navarro et al., 2020), mapping (Bovenga et al., 2012) and long-term monitoring (Bekaert et al., 2020; Casagli et al 2023). However, the regional investigation of mass movements through multitemporal InSAR techniques is still limited by the satellite orbital

geometry, resulting in sparse coherent scatterers in unfavourably oriented slopes and in areas subjected to layover and shadowing, by decorrelation effects due to snow cover and dense vegetation, and by artifacts related to atmospheric phase delay and unwrapping errors (Wasowski and Bovenga, 2014; Murray et al., 2019; Crippa et al., 2021). Furthermore, mass movements often are, or become during critical stages, too rapid to be reliably captured by widely used C-band multitemporal InSAR products, yet too slow to be effectively detected through optical imagery or SAR amplitude analysis. Although this gap can be partially filled by using different radar frequencies (e.g. L band; Garcia-Davalillo et al., 2013; Strozzi et al., 2026), it is recognized that part of the information contained in SAR interferograms is lost in multitemporal processing (Monti-Guarnieri and Tebaldini, 2008).

In this context, standard dual-pass differential interferometry (DInSAR) can deliver spatially quasi-continuous deformation products (i.e. wrapped SAR interferograms). This is a valuable alternative to recognize and characterize landslides through the direct analysis of interferometric fringes and phase patterns (Handwerger et al., 2013; Bayer et al., 2018; Manconi et al., 2018; Dini et al., 2019; Squarzoni et al., 2020; Crippa et al., 2020). Sentinel-1 satellites boosted a renewed interest in "raw" C-band interferograms, thanks to the small and stable perpendicular baselines and the short revisit time, allowing to obtain highly coherent interferograms, able to capture mass movement dynamics in relation to climate forcing, also over large areas (Beckaert et al., 2020) even with complex kinematic, structural controls (Hu et al., 2019) and low signal-to-noise ratio as for slow rock slope deformations in alpine environments (Crippa et al., 2020; Manconi, 2021).

The massive data volume, technical complexity and required expertise have so far limited the exploitation of wide-area InSAR products. As in other image analysis applications, machine learning algorithms, and particularly deep learning models such as convolutional neural networks (CNNs), can help unlocking the potential of interferograms to detect and classify InSAR signals corresponding to landslides (Zhu et al., 2021). The deep learning approaches adopted for the automated mapping of slow landslides depend on the desired mapping task (i.e. detection, classification, segmentation) and the exploited InSAR products. Most published deep learning applications to landslide mapping use multitemporal InSAR products (Zhang et al., 2025; Zhou et al., 2025), thus suffering the intrinsic detection limitations of these data.

Recently, few attempts have been made in the geoscience communities to automatically detect surface deformation fringes (Silva et al., 2022), subsidence troughs (Rotter and Muron, 2021), and to classify co-seismic (Brengman and Barnhart, 2021) or volcanic deformations (Anantrasirichai et al., 2018). Nevertheless, applications of deep learning to the tasks of detecting, classifying and segmenting active landslides in wrapped interferograms are still very few and represent a largely unexplored frontier, with strong potential for automated multi-temporal mapping and monitoring of landslides. Recently, some successful attempts have been made to apply CNN models to the segmentation of slow landslides in wrapped SAR interferograms (FCN, DeepLabV3 and U-Net-like models; Bralet et al., 2024; MB-Net; Zhang et al. (2024); U-Net, Dasser et al., 2026). Fu et al. (2022) proposed to automatically detect landslides in SAR interferograms using YOLO model applied to large stacks of phase gradient maps, advancing a routine, short-term assessment of active landslide occurrence. Despite these technological strides, the automatic identification of landslide-related displacement signals in individual raw, wrapped SAR interferograms is still

elusive. Fringes caused by slope deformation are frequently distorted or masked by noise and decorrelation, hindering automated extraction.

In this work we propose a deep learning framework for the automated detection and classification of slow landslides displacements in raw DInSAR products, in order to: a) exploit the rich information content of DInSAR phase signal; b) deliver rapid outputs to human experts in charge of wide-area landslide inventory update and hazard assessment through object detection and classification; c) use free and routinely available SAR imagery to maximize the model applicability to long-term monitoring; d) capture landslide processes over a range of spatial and temporal scales, to foster model applicability to different mass movement types; e) include strong geomorphological constraints.

To fulfil these objectives, we developed an object detection framework based on a YOLO architecture. We opted for bounding boxes rather than semantic segmentation to avoid the inherent ambiguity and high uncertainty associated with manual pixel-wise contouring during training label generation in wrapped SAR data (Dasser et al., 2026). To avoid any data loss prior to feature extraction, we preserved the input data at its original 16-bit radiometric depth, retaining the full information content of the phase signal. Finally, by simultaneously ingesting three distinct layers—wrapped interferograms, a SAR reliability index, and a layer synthesising terrain morphology—the model is designed to intercept deformation signals within their true physical context, closely emulating the assessment process of a human expert.

The paper is organised as follows: Section 2 describes the geomorphological and geological setting of the test area. Section 3 details the proposed methodology, including the preparation of the multi-layered input data, the ground-truth annotation workflow, and the customized YOLO-based deep learning architecture. Section 4 presents the model's results, providing both a quantitative evaluation of its detection performance and a qualitative geomorphological interpretation of the predictions. Section 5 discusses the implications of the findings, the model's limitations, generalization capabilities, and potential operational uses, while Section 6 summarizes the main conclusions.

2 Test area

We developed our approach in a study area covering approximately 1200 km² in the central sector of the Northern Apennines (Emilia-Romagna, Italy), located southwest of the city of Bologna and centered on the Reno River catchment, with extensions into adjacent basins (Figure 1). Elevations range from about 70 m a.s.l. in the foothill sector to over 1000 m a.s.l. along the southern boundary, reflecting a transition from low relief to rugged mountainous terrain. The Reno River drains the area through an intramontane valley where several orders of fluvial terraces, ranging from Middle Pleistocene to Holocene in age, document the long-term interaction between tectonics, climate fluctuations, and river incision (Picotti and Pazzaglia, 2008).

The regional climate is Mediterranean with continental influences, characterized by mean annual precipitation of 900 to 1600 mm depending on altitude. Rainfall is concentrated in spring and autumn, separated by relatively dry summers and moderately wet winters, partly influenced by snowfall at higher elevations. This seasonal distribution plays a role in slope instability, with

landslide activity typically peaking from late winter to early spring in response to prolonged or intense rainfall on already saturated soils (Bayer et al., 2018).

From a geological perspective, the area is dominated by Formations belonging to both the Ligurian and Epiligurian domains, consisting largely of chaotic clay-rich weak rocks (clay-shales and marly complexes) and turbiditic flysch successions (Boccaletti et al., 2011). Clay-shales are characterized by a highly tectonized structure and weak mechanical properties, further compromised near the surface by weathering, swelling, and stress relief processes (Pini, 1999). These units frequently include floating-in-matrix blocks of limestone and/or sandstone remnants of the original bedding structure. In contrast, flysch rocks consist of alternating sandstones and marls, forming stratified successions with variable mechanical behaviour depending on lithological composition, bedding orientation, and tectonic deformation (Valloni and Zuffa, 1984).

The study area is highly prone to mass movements, with the regional inventory documenting about 10,000 mapped landslide deposits (R.E.R., 2025). Landsliding is closely linked to bedrock properties. In clay-rich weak rocks, large and persistent earthflows are widespread (Simoni et al., 2013), typically exhibiting a characteristic morphology with source, transport, and depositional zones. These phenomena often originate as rotational or translational slides in the upper slope and evolve downslope into flow-like movements, forming complex landslide systems. Earthflows generally move at very slow rates (mm/yr to cm/yr) during long dormant phases that may last centuries but can undergo rapid reactivations with velocities reaching meters per hour or even higher during catastrophic events. In flysch terrains, slope failures are more heterogeneous and include rotational and translational slides (Berti et al., 2017), occasionally transitioning into flow-like behaviour downslope, as well as localized rockfalls controlled by slope geometry and structural discontinuities. Overall, the study area represents a geomorphologically dynamic environment where tectonics is active, and landsliding represents one of the main landscape-shaping agents.

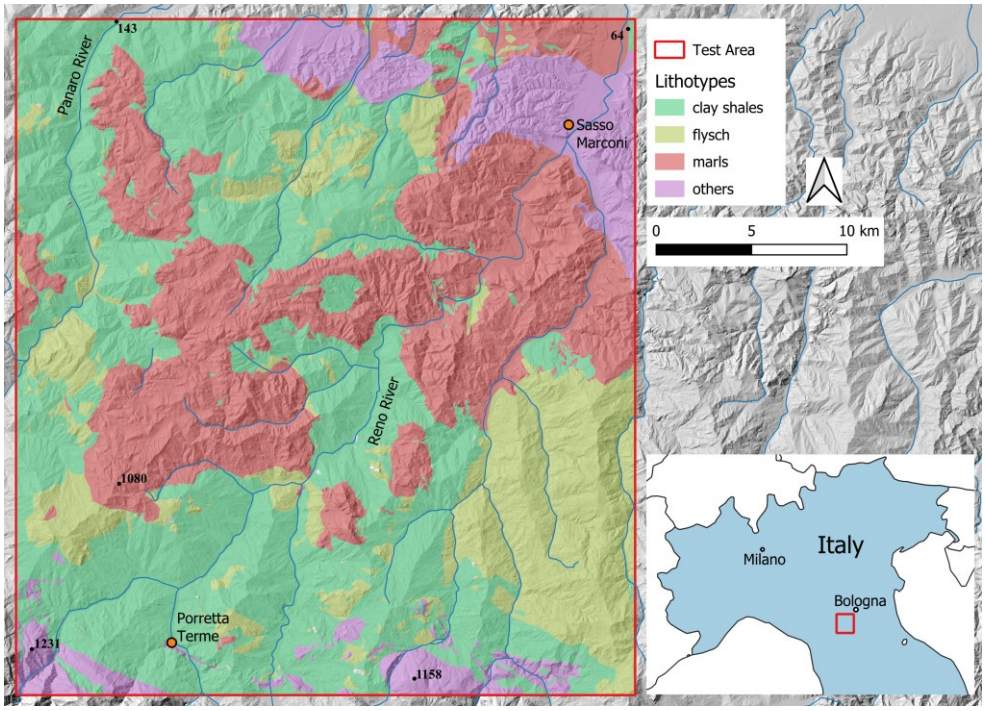

Figure 1. Location and lithological sketch of the study area.

3 Methodology and input layers

3.1 Model architecture

We propose a supervised deep learning framework to automatically detect and classify slow-moving landslides in satellite SAR wrapped interferograms, to exploit the potential of DinSAR phase signals derived from free, routinely available C-band SAR imagery provided by the Sentinel-1 mission.

We use a YOLO (You Only Look Once) Version 3, a real-time, fast and accurate object detector originally developed to operate with RGB optical images (Redmond and Farhadi, 2018) and modified to ingest 16-bit input layers, characterized by a 3-scale fully convolutional architecture that allows identifying objects of variable size in their context in one step. Our model

is fed by a stack of three layers, including wrapped DInSAR phase, a SAR sensitivity index layer, and a composite geomorphometric layer, in the attempt to emulate human expert interpretation.

Our workflow is divided into four main steps: (i) data selection and preprocessing, where the multi-layered input is generated; (ii) data annotation, involving the manual definition of ground truth bounding boxes by domain experts; (iii) model training, where a YOLO-based architecture learns to extract and classify spatial features associated with slope instabilities; and (iv) model evaluation, dedicated to assessing the detection performance using standard computer vision metrics.

3.2 Model input layers

To provide the neural network with the contextual data that a geomorphologist relies upon, we constructed a customised three-band input stack. This composite input replaces the standard RGB channels typically used in object detection models. The first layer consists of the wrapped InSAR interferogram, which contains the signal mapping the displacement (i.e. the interferometric fringes). The second layer is a sensitivity index, derived from a combination of interferometric coherence and SAR imaging geometric properties, which helps the neural network distinguishing the areas affected by severe decorrelation, low displacement sensitivity, or geometric distortions like layover and shadow. The third layer synthesise a set of geomorphometric indices able to discriminate spatial domains associated with active slow-moving landslides

3.2.1 Wrapped InSAR interferograms

The adopted methodology is based on the application of DInSAR using the conventional two-pass approach. InSAR enables the measurement of surface deformation through the analysis of phase differences between radar images acquired along the same orbit, although the technique is inherently affected by limitations such as phase ambiguity (Chen et al., 2001), decorrelation (Zebker et al., 1992), and atmospheric and orbital artifacts (Tarayre et al., 1996). To mitigate these effects, we selected interferograms characterized by short temporal baselines and small perpendicular baselines to preserve coherence and ensure the reliability of the interferometric signal. We use C-band Sentinel-1 images acquired in Interferometric Wide Swath (IW) mode and Single Look Complex (SLC) format in both ascending (track 117) and descending (track 95) orbits. Overall, 1042 interferograms were generated, 585 in ascending and 457 in descending orbits, spanning January 2016 to April 2025 with temporal baselines ranging from 6 to 30 days and perpendicular baselines smaller than 200 m approx. We carried out the processing using the open-source GMTSAR software (Sandwell et al., 2011), following a standardized workflow. We first co-registered SAR images to a single master image selected near the temporal midpoint to minimize geometric distortions. We then projected a digital elevation model, 10 m resolution (R.E.R., 2007), into radar geometry to estimate and remove the topographic phase component (Massonnet and Feigl, 1998). We subsequently generated interferograms by pairing co-registered images with different temporal baselines, maintaining the phase in wrapped form (modulo 2π). To enhance the signal-to-noise ratio, we first filtered the interferograms through a 100 m window spatial Gaussian filter, which reduces high-frequency noise. Then, the adaptive spectral Goldstein filter (Goldstein and Werner, 1998) was applied using a 32-pixel-sized

window and an alpha exponent of 1. No specific filtering for atmospheric phase signal removal was applied. Coherence was calculated using a boxcar filter to assess the reliability of the wrapped phase information and identify decorrelated areas. After careful manual inspection of all the generated interferograms, we selected those characterized by high coherence, limited local atmospheric disturbances, low residual noise and high signal-to-noise ratio at the slope scale, which is essential for reliable expert interpretation. Of the 1042 processed interferograms, we retained 56 meeting these criteria for further analysis (Table S1). Selected interferograms typically exhibit well-preserved phase information and a generally high level of coherence across the study area, as shown in the example reported in Figure 4 and other interferograms reported in the Supplementary material. No evident long-wavelength orbital ramps nor ionospheric effects are observed, and residual atmospheric effects appear limited, with no prominent localized phase anomalies affecting the scene. Overall, the interferogram provides a high-quality phase signal suitable for slope-scale geomorphological interpretation. Finally, we geocoded the interferograms with a ground sampling distance of 15 m, suitable to capture the studied processes at the typical spatial resolution of Sentinel-1 IW (Interferometric Wide Swath) data and exported them to a GIS environment. This workflow enabled the generation of robust interferometric datasets for the identification and monitoring of active gravitational slope processes.

3.2.2 InSAR Sensitivity Layer

We designed the InSAR sensitivity layer to support the neural network learning process by weighting the DInSAR phase according to the reliability of its information content related to the potential ground displacement. The quality of the displacement signal recorded in the DInSAR phase depends both on the decorrelation noise affecting the InSAR signal and on geometrical factors. Specifically, the degree of correlation between the SAR images composing the InSAR pair defines the signal-to-noise ratio of the phase fringes, which is estimated through the InSAR coherence (Zebker and Villasenor, 1992). The coherence of an interferogram relies on pixel back-scattering characteristics remaining unchanged between two images. Growing vegetation, snow cover, flooding, and rapid ground deformation can cause decorrelation on an interferogram, that is, a loss of signal coherence between acquisitions. In steep terrain or highly deforming areas, phase gradients can exceed a radar wavelength per pixel, reducing coherence. Moreover, the geometrical distortions related to the SAR imaging and the ground topography limit both the sensitivity to the ground motion and the visibility of the area (Wasowski and Bovenga, 2022). DInSAR fringes related to ground displacements depend on how much of the movement occurs in the direction of the satellite's LOS. Therefore, to accurately detect ground movements, it is important for the sensor's LOS to be as aligned as possible with the direction of the movement; otherwise, the fringe pattern will be less effective at showing the ground's changes, thus negatively impacting the recognition procedure. The Slope-to-LOS (S2L) index estimates the InSAR sensitivity to downslope movement and depends on the SAR acquisition geometry and ground slope orientation (provided by slope and aspect angles). It is defined as the projection of the unit vector directed along the slope towards decreasing gradients and the unit vector representing the LOS. S2L can be computed by using ancillary data (basically angles) coming from standard InSAR processing by using the following:

$$S2L = \sin(\beta)\cos(\vartheta) + \cos(\beta)\sin(\vartheta)\sin(\delta - \alpha) \quad (1)$$

where β and δ are, respectively, the slope and aspect angle derivable from a digital elevation map (DEM), α is the orbital heading angle, and ϑ is the incident angle defined as the angle between the SAR LOS and the normal vector to the ellipsoid. This S2L formulation coincides with the C-factor proposed in (Kalia et al., 2018; Van Natijne et al., 2022). S2L values close to 1 indicate a perfect alignment between LOS and local slope, on the contrary, S2L values close to 0 mean that just a small fraction of the ground displacement is detected by InSAR, leading to a weak and unfavourable signal to be processed by the neural network model. The InSAR Sensitivity Layer (ISL) is defined as the product of S2L by the coherence map and provides a pixel-based index that properly weights the corresponding InSAR phase value, where 0 means a useless phase (due to noise and/or geometrical distortions), while 1 means noise-free and ideal view conditions. Moreover, since very low coherence (below 0.3) values are generally biased and correspond to useless InSAR phase (Touzi et al., 1999), we introduced a sigmoid function (W_{Coh}) as a weight for the coherence to aid the neural network model to learn just from reliable phase values:

$$S2L = \sin(\beta)\cos(\vartheta) + \cos(\beta)\sin(\vartheta)\sin(\delta - \alpha) \quad (2)$$

with:

$$W_{Coh}(x,y) = \frac{1}{1+e^{\left(-k(\gamma(x,y)-\gamma_M)\right)}} \quad (3)$$

where k is the sigmoid steepness and γ_M is the sigmoid midpoint. The data in input required to derive the ISL are: i) the coherence map coming from the standard InSAR processing; ii) the incident angle ϑ for each pixel of the reference (master) image, computed wrt the ellipsoid; iii) a ground digital elevation map (DEM) needed to derive slope and aspect angles. Figure 2 sketches an example of input products, namely a DEM (a), an incident angle map (b), and a coherence map (c), intermediate products, namely the slope (d) and aspect maps (e), and the S2L map (f), and their combination for generating the ISL map in output (g). The products refer to the interferometric pair made by two Sentinel-1 images acquired over the test area. As expected, the ISM shows low values where both coherence and sensitivity to displacement are low.

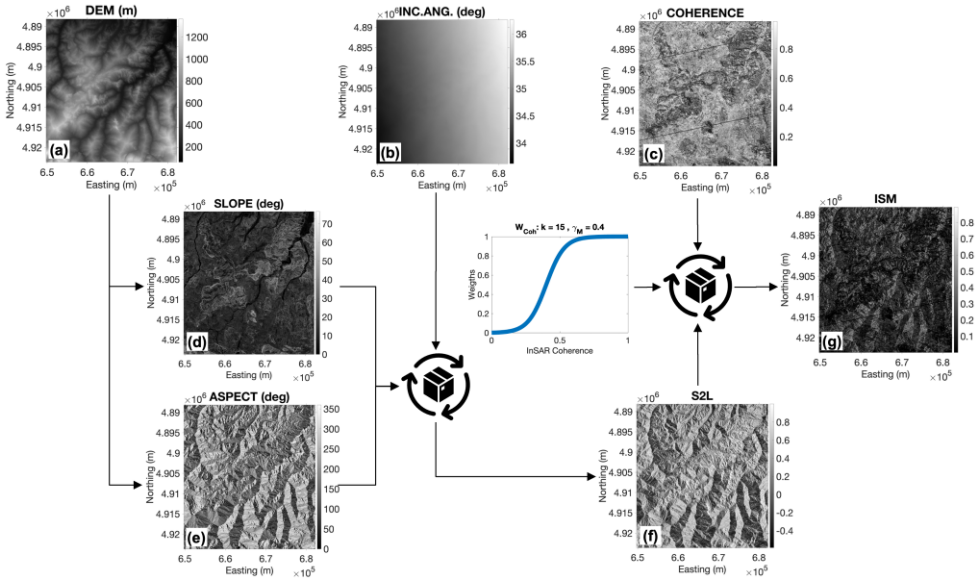

Figure 2. Examples of input products (a, b, c), intermediate products (d, e, f), and their combination for generating the InSAR Sensitivity Layer ISL (g). The products refer to the interferometric pair made by two Sentinel-1 images acquired over the test area on 4 and 10 December 2019.

3.2.3. Geomorphometric layer

To enhance the neural network's ability to emulate human interpretation in detecting signals corresponding to active slow-moving landslide areas, we carried out a geomorphometric characterization of the study area, based on the analysis of a Digital Elevation Model (Hengl and Reuter, 2008; Gessler et al 2009). Using a 10m-resolution Digital Elevation Model available for the Emilia-Romagna region (R.E.R., 2007), resampled to 15 m to be consistent with the SAR wrapped interferogram rasters, we computed several morphometric variables for each study area, including slope, aspect, profile and plan curvature, convexity, terrain roughness index (TRI), and topographic wetness index (TWI) (Gessler et al 2009), using the open-source SAGA GIS Terrain Analysis module. We selected these variables based on their known relevance to mass movement processes, and the corresponding computational algorithms were optimized—particularly in terms of window size—to fit the typical scale of landscape features in the area. The frequency distributions of single morphometric variables do not show significant differences within and outside the landslide areas portrayed in the published Emilia-Romagna Regional Inventory

(R.E.R., 2024) and the Italian Landslide Inventory (IFFI, 2024). Therefore, we explored their relationships through a Principal Component Analysis (PCA, Hotelling, 1933). PCA is conceived to explore and interpret a set of data by reducing the dimensionality of their variables, i.e. by finding new variables that are linearly related to the original ones, maximize their variance, and are uncorrelated with each other. In our analysis, we considered the principal component PC1, accounting for the larger amount of variance for different combinations of the set of morphometric variables. Following several tests, we selected the PC1 derived from the configuration including slope gradient, convexity, TRI and TWI (Figure 3) as it provided the most consistent and informative representation of geomorphological variability. The obtained PC1 loadings were 0.580 (slope), 0.518 (TRI), -0.543 (TWI), and 0.318 (convexity), respectively. Overall, PC1 discriminates between steep, rough slopes (Slope, TRI, convexity associated with positive loadings) and flat or concave, potentially humid areas (TWI associated with negative loading). This PC1 layer allows to summarize the signatures of topography associated (or not) to landslide classes (Figure 3), providing the neural network with an additional layer of context information usually considered (also implicitly) in the human geomorphological interpretation process.

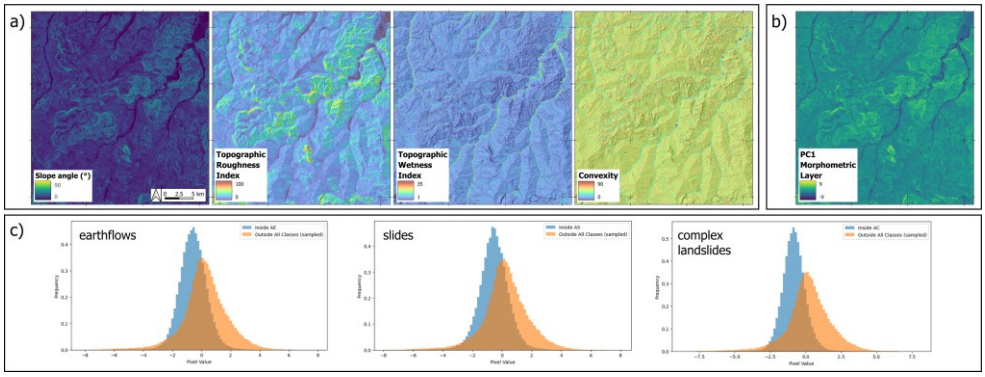

Figure 3. Morphometric variables selected to discriminate active areas from the surroundings (a), summarized by the Principal Component PC1 (b). PC1 frequency distributions inside and outside landslides mapped in the landslide inventory (R.E.R., 2024) and belonging to different landslide types (c).

3.3 Neural network training and testing dataset

To train and test our neural network, we used the comprehensive dataset of DInSAR wrapped phase signals constructed by Reyes-Carmona et al. (2026). This is the only publicly available dataset specifically developed for deep learning models aimed at the detection of mass movements in SAR interferograms in the form of bounding boxes, different from the dataset ISSLIDE

(Bralet et al, 2024), that is aimed at semantic segmentation models. The dataset contains approximately 5000 expert-annotated DInSAR wrapped phase signals associated with different mass movement types identified over two wide test areas covering the Northern Apennine and Central Alps of Italy. Active mass movements were recognized in multiple SAR interferograms generated over different temporal baselines, classified according to geomorphological criteria and with the support of ancillary datasets. Each label object in the dataset is made of (Reyes-Carmona et al., 2026): a) a rectangular box bounding the wrapped phase signal corresponding to an active mass movement process; b) the corresponding wrapped interferogram patch; c) associated attributes (process class, reference interferogram, temporal baseline, etc.). Bounding boxes were manually delineated around recognizable displacement patterns interpreted as landslide-related signals.

This interpretation was supported by independent landslide inventories, high-resolution orthophotos, and DEM-derived products, which provided the geomorphological context required to distinguish genuine deformation from interferometric artifacts. Specifically, the ancillary data comprised landslide inventories from the Emilia-Romagna Regional Inventory (RER, 2024) and the Italian Landslide Inventory (IFFI, 2024), as well as orthophotos (2015–2024) and DEMs with a spatial resolution of 10 m or, where available, 0.5 m, retrieved from the Emilia-Romagna Geoportal (https://geoportale.regione.emilia-romagna.it/). The geomorphological plausibility of each candidate wrapped phase signal was assessed using the ancillary datasets, and its temporal persistence was verified across multiple interferograms to exclude transient artifacts. The annotated features were subsequently classified according to landslide type and involved lithotype. In the study area, three classes were distinguished: earthflows in clay shales (CF), earthslides in shales/marls (CS), and rockslides in flysch rocks (FS) (Figure 4). In addition, common interferometric artifacts that may locally resemble ground deformation, such as small-scale atmospheric disturbances and topographic residuals, were annotated to reduce false positives during model inference (Figure 4). Field observations at selected landslide sites further strengthened the interpretation and provided additional support for ground-truth validation.

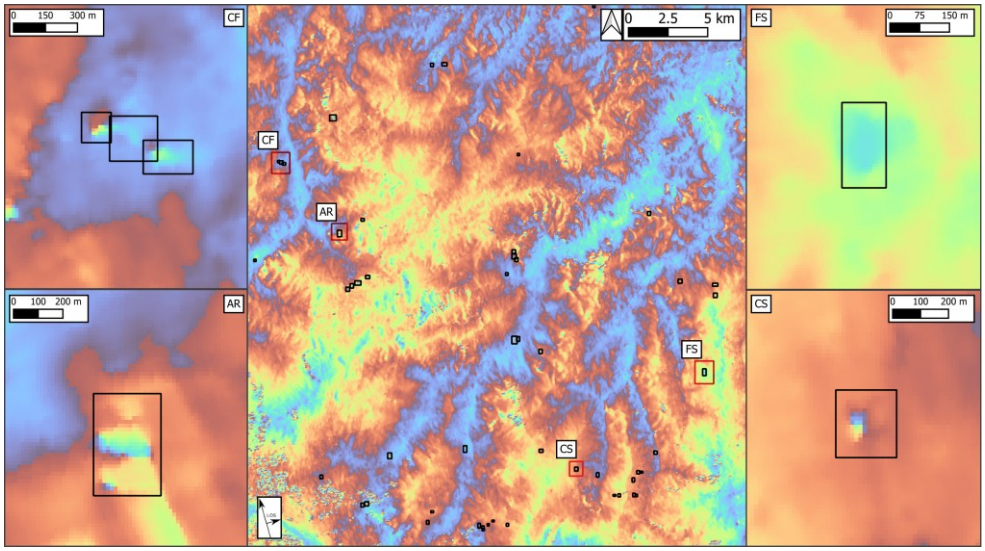

Figure 4. Wrapped interferogram of the test area for the ascending acquisition pair 22/03/2021–28/03/2021, showing the interpreted bounding boxes (centre). Enlarged examples of the identified phase signals are displayed in the insets, showing an earthflow in clay shales (CF), an artifact (AR), a rockslide affecting flysch rocks (FS), and an earthslide in shales/marls (CS).

Commented [CR1]: Put the label of landslide type on each image (only with numbers is a bit difficult to follow)

3.4 Model setup, training, validation, and testing

Given the large spatial dimensions of the original interferograms and the input size constraints of the YOLO architecture, we divided them into non-overlapping patches of a fixed size of 160 x 160 pixels (corresponding to 2,400 x 2,400 m).

We then optimised the anchor boxes—pre-defined bounding box shapes used by the network to predict object locations—using a k-means clustering algorithm applied to our specific ground truth training set. This adaptation ensures that the network is highly sensitive to the typical spatial dimensions and aspect ratios of landslide deformation patterns in the selected study area and in the patches.

We then collected the resulting image tiles and their corresponding bounding box annotations to form the final dataset.

We randomly partitioned the set of tiles into three distinct subsets: 80% for training (579 tiles), 10% for validation (71 tiles) and 10% for testing (73 tiles). We trained the network using the standard Adam optimiser. To mitigate overfitting while respecting the unique physical properties of SAR imagery, we selected a domain-specific data augmentation strategy. We applied spatial transformations (e.g., flipping, random cropping) while we limited radiometric distortions exclusively to random multiplicative scaling and shifting to mimic baseline phase variations, avoiding standard optical colour jittering.

During the training phase, the 10% subset served as a validation set, enabling rapid performance checks, including hyperparameter tuning and early stopping in case of critical overfitting by monitoring the loss function. Upon completion of the training process, we used the 10% unseen test dataset to evaluate the final detection performance.

We based our quantitative analysis on metrics derived from the confusion matrix (e.g. Goodfellow et al., 2016). In this context, True Positives (TP) correspond to the correct spatial localisation of the bounding box evaluated via an Intersection over Union (IoU) threshold and the correct labelling of the kinematic process generating the displacement. False Negatives (FN) represent real ground displacements that the model failed to intercept. False Positives (FP) indicate either a bounding box with inaccurate dimensions or positioning (falling below the IoU threshold), a misclassified displacement type, or a detection where no real displacement exists. True Negatives (TN), areas without active displacement correctly identified as stable background, are excluded from the evaluation to avoid artificially inflating the overall performance scores, given the highly imbalanced ratio between stable and unstable areas captured by the interferograms. We focused on two standard object detection metrics (Goodfellow et al., 2016; Padilla et al., 2020): the F1-score (which provides a single metric balancing the model's ability to find real displacements against the rate of false alarms) and the mean Average Precision (mAP, representing the global accuracy of the model across multiple confidence levels). For both metrics, we adopted a minimum IoU threshold of 0.5 between ground truth and model predictions to assign a TP.

4 Results

This section presents the outcomes of the proposed YOLO-based detection model, structured into a quantitative and qualitative assessment. The quantitative evaluation follows the standard machine learning best practices for object detection . The qualitative evaluation consists of domain expert critically exam of the model's misclassifications through visual analysis conducted from a geomorphological perspective of the False Positives and False Negatives—to understand the physical, topographic, and interferometric drivers behind the potential network's errors.

4.1 Detection/classification training, validation and testing

Figure 5 illustrates the training and validation dynamics of the YOLO-based model over the training epochs. Inset (a) presents the Total Loss, which exhibits a sharp initial decline followed by a stable plateau. The validation loss tracks the training loss throughout the process, indicating model convergence without significant overfitting. Inset (b) displays the learning rate schedule, showing the smooth decay strategy employed to fine-tune the network's weights.Insets (c) through (f) break down the loss into its constituent components. Both the Box Loss (c) and Class Loss (f) decrease rapidly and stabilize at low values, demonstrating the network's efficiency in precisely localizing deformation bounding boxes and correctly classifying the different mass movement types. The Object Loss (d) shows an initial rise as the model begins proposing candidate regions, followed by a steady, consistent decline as the network learns to discern true displacement signals from the background. Similarly, the No-Object Loss (e) drops sharply and remains minimized, highlighting the model's robustness in filtering out

stable terrain and background noise. Early stopping occurred at epoch 631 after a patience of 30 epochs. Total loss resulted in 2.1. Overall, the consistent alignment between the training and validation curves across all metrics confirms the efficacy of the hyperparameters and data augmentation strategies.

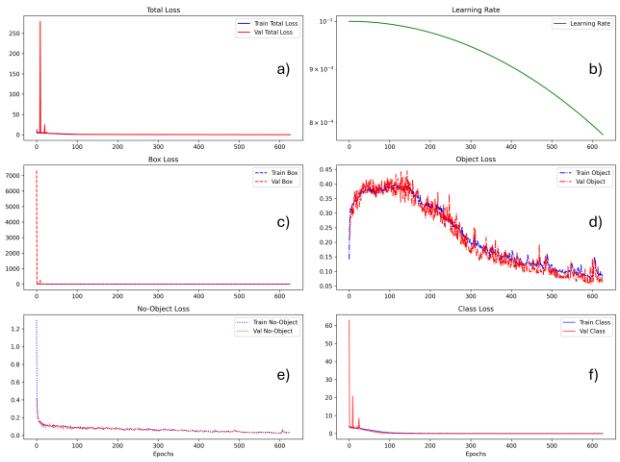

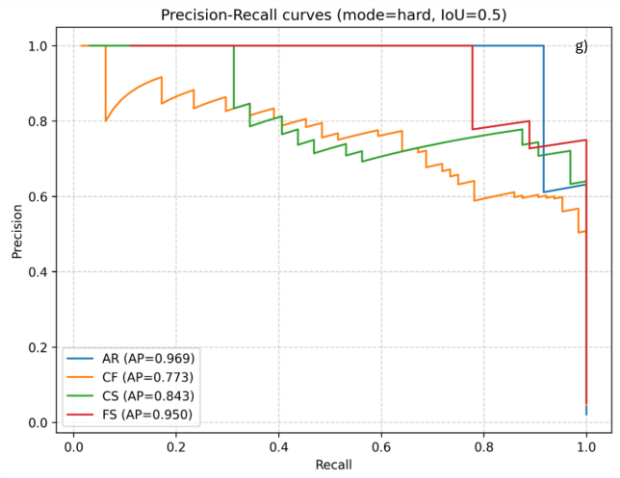

Figure 5. Panels (a) through (f) display the training and validation metrics over the optimization epochs, including the Total Loss (a), the learning rate schedule (b), and the specific loss components: Box Loss (c), Object Loss (d), No-Object Loss (e), and Class Loss (f). Panel (g) presents the Precision-Recall curves evaluated on the independent test set (IoU = 0.5) for the four classified mass movement types.

To evaluate the quantitative performance of the model, we applied a standard IoU threshold of 0.5 paired with a confidence threshold of 0.81, a combination identified as optimal for maximizing the evaluation metrics. Under these set parameters, the model achieved a global mAP of 0.883 (Figure 5g). The overall detection performance yielded a Precision of 0.630 and a high Recall of 0.93, resulting in a global F1-score of 0.751. This high Recall underscores the network's effectiveness in identifying landslide displacements (successfully detecting 109 True Positives out of 117 total Ground Truth instances, leaving 8 False Negatives), while maintaining a reasonable rate of potential False Positives (64).

A detailed breakdown of the model's performance across the different identified classes is summarized in Table 1.

Table 1. Per-class quantitative results evaluated at a confidence score of 0.81 and an IoU threshold of 0.5. (GT = Ground Truth; TP = True Positives; FP = False Positives; FN = False Negatives; P = Precision; R = Recall; #GT = Ground Truth; #PRED = Raw Predictions (before the application of the confidence score threshold)

Class	AP	TP	FP	FN	P	R	#GT	#PRED
AR	0.969	12	7	0	0.632	1.000	12	562
CF	0.773	57	38	7	0.600	0.891	64	1308
CS	0.843	31	12	1	0.721	0.969	32	579
FS	0.950	9	7	0	0.562	1.000	9	174

Figure 5g shows the Precision-Recall curves for all classes. The graph is the markedly irregular, step-like trend (sawtooth pattern) across all curves. This morphology is a consequence of the limited size of the test set, and the step-like progression is expected in a specialized domain with numerically limited test sets. Nevertheless, every single processed prediction generates a discrete, macroscopic variation along the axes. The AR and FS classes exhibit the most favourable curve profiles. Both maintain a Precision of 1.0 across a large portion of the Recall axis (up to 0.9 for AR and approximately 0.78 for FS). This indicates the scarcity of data in the classes but also that the model's highest-confidence predictions for these classes are highly accurate and free of False Positives. The vertical decline in Precision occurs only at the extreme right of the graph, confirming that the model introduces errors exclusively at minimal confidence thresholds, after most true targets have already been retrieved. The CS class demonstrates an intermediate behaviour. The curve remains stable at 1.0 Precision up to a Recall value of approximately 0.3, at which point the initial high-confidence False Positives are introduced. Precision degrades

progressively in proportion to the increase in Recall, ultimately yielding a final Average Precision (AP) of 0.843. Visually and quantitatively, the CS class represents the most complex category. The initial decline in Precision occurs early (Recall < 0.1), indicating that the model generates False Positives even among predictions assigned a high confidence score. The higher density of the sawtooth variations along the entire curve reflects the larger volume of data processed for this specific class (which contains the highest number of Ground Truths and total predictions). Despite the early drop, the curve stabilizes, ensuring a target retrieval rate that brings the final AP to 0.773. Overall, the curves confirm the network's capability to isolate the targeted physical features. The observed decreases in Precision—particularly for the CS and CF classes—document the inclusion of False Positives as the confidence threshold is lowered. This represents a necessary and expected trade-off to maximize Recall in the context of anomaly and deformation detection tasks. The model's misclassifications—both False Positives and False Negatives—do not exhibit significant spatial and temporal clustering. Errors appear to be randomly distributed across the entire study area and the period of study. This lack of localized error clustering suggests that the network's performance is not systematically biased by specific regional topographic features or localized interferometric decorrelation phenomena.

Figure 6 illustrates several examples of the comparison between ground truth labels (red dashed boxes) and the model predictions (solid black boxes). In the (a) panel, two CS signals are correctly mapped. In panel (b), a small CF on the left is correctly detected, while a larger CF on the right is wrongly interpreted by the model as two separate CFs (resulting in two FP and one FN, as neither prediction adequately matches the ground truth). Similarly, the (c) panel shows one CF wrongly mapped by two overlapping CF bounding boxes; since the overlap fails the IoU threshold, this also yields two FP and one FN. The (b) panel presents a more complex scenario: one CF and one FS are correctly mapped, another CF and FS could potentially be considered TP depending on the chosen IoU threshold, and one FS is a clear FP. The (e) panel contains at least one CF FN, one FS FP, and four well-mapped displacements. Finally, the (f) panel displays one FS FN alongside four properly mapped displacements. Operationally, False Negatives represent the worst-case scenario (missed hazards), while for some False Positives, there is a degree of interpretative uncertainty. This specific issue is further addressed in the following paragraph.

4.2 Geomorphological interpretation

The model provides datasets of classified mass movement areas active in each considered time frame. Together with the objectness scores, bounding box offsets and class probabilities, it is important to understand what geomorphological and interferometric conditions may lead to false negative or false positive detections. We carried out this investigation by visually inspecting false predictions. When comparing model results with the ground truth (i.e. the bounding boxes in the dataset used for testing), one should clearly bear in mind that in our case, ground truth is represented by the result of the work carried out by expert interpreters on unwrapped interferograms with the aid of geological and geomorphological information. The criteria that guided the interpretation are explained in the methodological sections above, however the size and positioning of the polygon are subject to inevitable subjectivity and are therefore associated with some uncertainty. The identification of the

signal itself is sometimes associated with uncertainty since the interpreter chooses the colour scale and sees accordingly. Weak signals of small size are more likely to be neglected because they are barely visible and/or mistaken for residual noise.

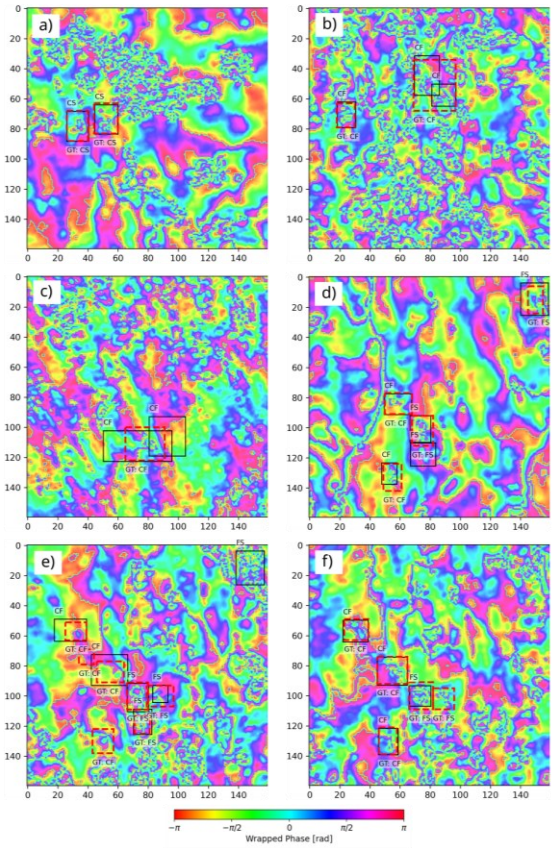

Figure 6. A high-contrast, customized visual rendering of the interferograms, featuring sharpened boundaries between phase values, allows enhancing the visual prominence of subtle deformation fringe patterns and assists human operators in validating

YOLO detections (solid black boxes) against ground truth labels (red dashed boxes) across various noise conditions. The panels refer to the following temporal baselines and acquisition years, all from ascending orbits: (a) 6-day, 2020; (b) 6-day, 2018; (c) 6-day, 2017; (d) 6-day, 2021; (e) 6-day, 2018; and (f) 12-day, 2018.

Table 1 reports the result of our exercise and clearly shows that FP significantly outnumber FN (i.e., 64 FP and 8 FN for the confidence score of 0.81). Given the IoU metric we use to measure the model performance, single deformation signals can be associated to 1, 2 or even 3 false predictions. The number of deformation signals associated with false model predictions is therefore relatively small. Nevertheless, we tried to select examples illustrating all possible types of false predictions that can be encountered.

Figure 7 shows a gentle NE-facing slope made of Clay Shales where elongated earthflow deposits side by side can be recognized. Two deformation signals can be seen in the central part of two of them (Fig. 7a, b). Not only the model correctly identifies the two CF signals, but it maps them very accurately when compared to the bounding boxes drawn by the interpreter. It detects also a third signal classified as earth slide (CS) along the stream bank, in the lower part of the slope. It corresponds to a mapped landslide associated to recurring interferometric signals (Fig. 7c) where vegetation is scarce or absent, as opposed to surrounding slopes (Fig. 7d). All elements indicate that the deformation could be progressing during the considered time frame, but the interpreter missed the phase difference signal which is, in fact, weak and difficult to recognize (Fig. 7b).

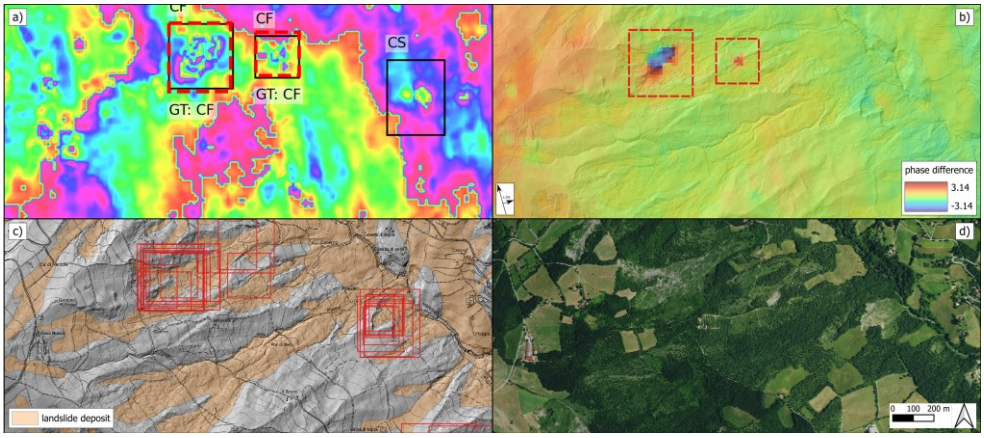

Figure 7. Comparison of model predictions and reference data for an example including of 2 TP and 1 FP. (a) Enhanced YOLO visualization, with predicted bounding boxes shown as black solid outlines and ground-truth annotations as red dashed outlines; (b) corresponding wrapped interferogram (ascending acquisition, 01–07/03/2017) with interpreted bounding boxes; (c) hillshade map showing inventoried landslide deposits and all multi-temporal annotations; and (d) 2018 aerial photograph.

Figure 8 illustrates a rather complex situation encountered across a ridge running in N-S direction, close to the SE corner of our study area (Figure 1). Many landslide deposits are mapped in the inventory (Figure 8e) and multiple deformation signals are recognized by the interpreter in the two interferograms reported here (Figure 8b, d). The classification of the signals made by the interpreter depends on both morphology and bedrock lithotype. In the first time frame (Figure 8a, b), the model correctly identifies and classify the four mapped bounding boxes. It also identifies two FP along the E-facing slope. They are located on mapped landslide deposits where deformation signals have been mapped in multiple interferograms (Figure 8e), preceding and following. It can be imagined that the model recognized weak phase difference patterns which are hardly recognizable by human eye, with the color scale adopted here. In the second time frame (Figure 8c, d), together with 6 correctly identified and classified signals, we find a FP (CF) in the central-upper part of the area and a FN (CF) further south. For the FP, we can make considerations like those of the previous time frame. The FN, instead, represents a rather unique case: the signal is reasonably visible in the interferogram but the model fails the detection.

The final two examples (Figures 9 and 10) illustrate false predictions arising from disagreement between object size and positioning predicted by the model and corresponding bounding boxes drawn by the interpreter. The bounding box is identified on an earthflow and classified accordingly (i.e., CF) in both cases though the deformation involves the toe of a large phenomenon in the first case (Figure 9b) while it is generalized across the entire earthflow, in the second case (Figure 10b). The deformation signal at the landslide toe is correctly identified and classified by the model but the size mismatch produces 1 FP and 1 FN in the metrics. Observing other signals mapped on the same area (Figure 9c) in different time frames, we notice a variability in size and positioning which characterize the spatial displacement pattern. The deformation signal mapped in Figure 10c and pertaining to an active earthflow includes at least a phase jump to testify relatively high displacement rates recorded by the 12-days interferogram. It has an oblique orientation with respect to the cartesian directions generating a relatively large bounding box. The model prediction consists of two smaller signals which originate 2 FP and 1 FN despite the correct classification.

Overall, the performance of the model can be described as very good with the largest number of false predictions associated to the size and positioning of the predicted and mapped bounding boxes (Figures 9 and 10). The second source of model errors is represented by FP predictions which, based on the visual inspection, correspond to actual poorly visible phase difference signals located on landslides (Figures 7 and 8). In these cases, FP are often true ones, missed in the mapping stage due to size, weakness or low signal/noise ratio of the phase signal. In such cases, the model apparently outperforms the interpreter. Finally, it is worth mentioning that FN cases are generally very few and we could isolate only one actually corresponding to a mapped deformation signals which went undetected by the model (Figures 8c, d).

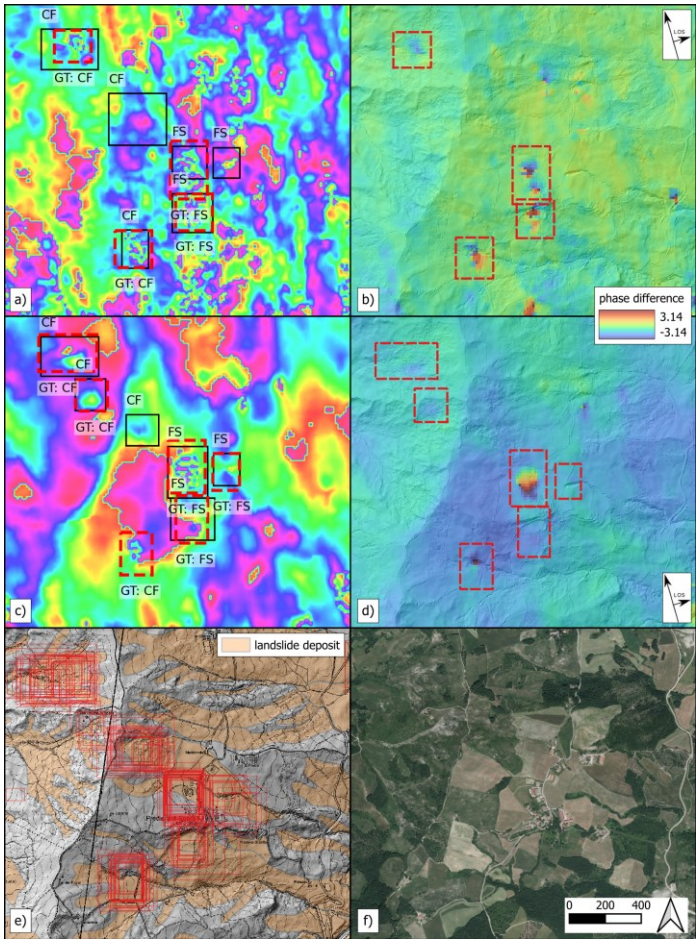

Figure 8. Comparison of model predictions and reference data for two representative examples. (a, c) Enhanced YOLO visualization, with predicted bounding boxes shown as black solid outlines and ground-truth annotations as red dashed outlines; (b, d) corresponding wrapped interferogram (ascending acquisition, 3-19/02/2019; 21-27/01/2020) with interpreted bounding boxes; (e) hillshade map showing inventoried landslide deposits and all multi-temporal annotations; and (f) 2020 aerial photograph. See text for descriptions.

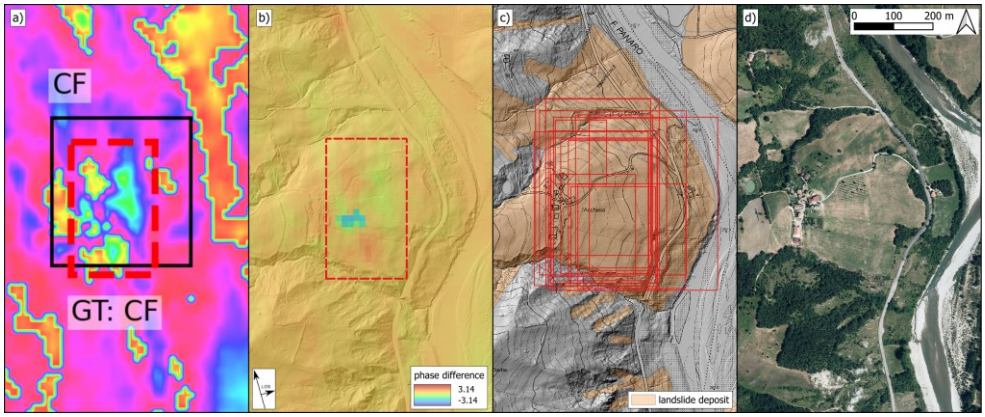

Figure 9. Comparison of model predictions and reference data for an example including of 1 FP and 1 FN. (a) Enhanced YOLO visualization, with predicted bounding boxes shown as black solid outlines and ground-truth annotations as red dashed outlines; (b) corresponding wrapped interferogram (ascending acquisition, 13-19/02/2019) with interpreted bounding boxes; (c) hillshade map showing inventoried landslide deposits and all multi-temporal annotations; (d) 2020 aerial picture.

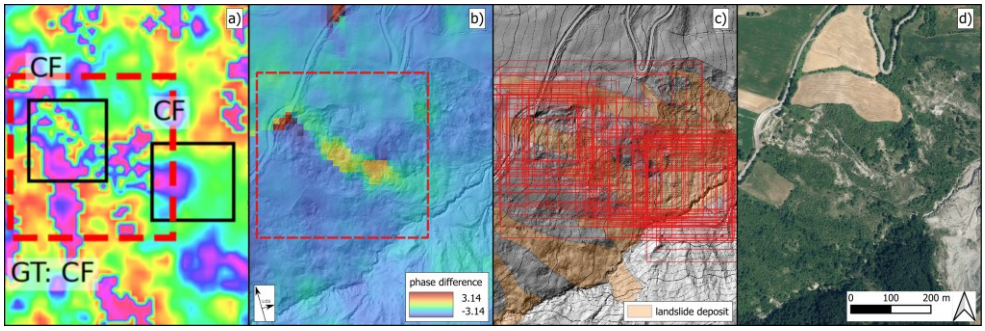

Figure 10. Comparison of model predictions and reference data for an example including of 2 FP and 1 FN. (a) Enhanced YOLO visualization, with predicted bounding boxes shown as black solid outlines and ground-truth annotations as red dashed outlines; (b) corresponding wrapped interferogram (ascending acquisition, 13-25/12/2016) with interpreted bounding boxes; (c) hillshade map showing inventoried landslide deposits and all multi-temporal annotations; and (d) 2018 aerial photograph.

5 Discussion

The application of artificial intelligence to the detection and classification of active slow landslide movements represents a major methodological challenge in the field of geohazard characterization and monitoring. Landslides are inherently heterogeneous, encompassing a wide range of types, processes, spatial extents, and displacement rates. A process-oriented perspective, grounded in geomorphological constraints, is therefore essential to guide model development and interpretation.

We demonstrated that routinely available, raw InSAR products have an information context that can be unravelled by modern deep learning techniques to detect active mass movements over wide areas in a fast and useful way. These results open interesting perspectives in both landslide science and practical applications, complementing and, in some cases, overcoming the multitemporal InSAR approaches which are commonly used nowadays. Despite being accurate at point locations, they inherently filter and simplify most of the original signal. Our findings acquire significance in the current scenario of SAR technology development, where new SAR missions providing free, routinely acquired, high-quality SAR imagery have just started (e.g. NISAR) or are upcoming (e.g. ROSE-L). In the near future, SAR data acquired at different wavelengths to overcome decorrelation (L/P bands) or increase displacement sensibility (X-band), as well as from mid-inclination orbits (e.g. the NIMBUS-IRIDE constellation) or multistatic configurations (e.g. the Harmony ESA Earth Explorer mission) to improve visibility on North-South slopes will become available, providing further opportunities for automated landslide detection.

We designed our model to intercept mass movement signals directly within minimally-filtered wrapped SAR interferograms, to unlock the potential of InSAR data, including noise. Rather than treating noise solely as a disturbance, the model leverages its hidden structured characteristics to enhance pattern recognition of other objects. This enables the detection of processes evolving over different scales and, under certain conditions, their classification. The system is not conceived as a fully automated inventory generator. Instead, it is designed to provide rapid, wide-area information for geohazard assessment, potentially supporting inventory updates and long-term monitoring strategies. A central objective is to deliver fast and geomorphologically interpretable outputs, ensuring that results are not only technically robust but also practically useful for operational decision-making.

While semantic segmentation is an increasingly popular choice in remote sensing for extracting exact landslide masks (e.g. Zhang et al,. 2024; Dasser et al., 2026), we pursued an object detection approach based on bounding boxes. This choice is motivated by the inherent complexity of wrapped DInSAR pahse. Human interpretation of interferometric fringes is affected by significant uncertainty (Dasser et al., 2026) due to decorrelation and phase artifacts, which often obscure the exact boundaries of a moving mass. Furthermore, the radiometric range and dynamics of the wrapped signal far exceed human visual capacity, making pixel-perfect manual contouring highly subjective. By predicting bounding boxes, we avoid forcing the network to learn from intrinsically uncertain boundaries, focusing instead on the robust localization and classification of the active processes.

5.1 Interpretation of results

Evaluation on the strictly unseen 10% Test Set (IoU = 0.5, confidence = 0.81) yielded a satisfactory mean Average Precision (mAP) of 0.8838 (Table 1, Fig. 6). The model achieved a remarkable global Recall of 0.9316 (missing only 8 out of 117 ground truth targets). While the Precision stood at 0.6301 due to a higher rate of False Positives, this behaviour is expected and contextually mitigable. In fact, while False Negatives are very few and correspond to certain missed detections relative to the reference dataset, the nature of False Positives is more ambiguous and deserves careful consideration.

The selection of an IoU threshold of 0.5 is a standard choice dictated by the need for literature comparability, yet it does not fully account for the specific nature of InSAR data. Unlike standard optical images where objects exhibit sharp and well-defined boundaries (e.g., buildings or vehicles), landslide deformation patterns manifest as interferometric fringes characterised by inherently fuzzy borders and gradual phase transitions towards stable ground. Consequently, a lower threshold would possibly be more representative: it would ensure the model is correctly credited for successfully localizing the core of the deformation signal, without being unduly penalized for slight spatial mismatches in the bounding box limits compared to the subjective human-annotated ground truth. Nevertheless, excessively low thresholds must be avoided, as they would complicate the correct matching between model predictions and ground truth labels in scenarios characterised by a high spatial density of adjacent mass movements, potentially leading to ambiguous evaluations. The selection of operational thresholds should not be driven exclusively by the maximisation of quantitative validation metrics. Rather, it must be weighed against the decision-making processes and the practical capacity of end-users to manage the resulting balance between False Positives and False Negatives.

A detailed geomorphological reassessment of the areas flagged as False Positives demonstrated that the model could intercept real ground displacements that were previously unrecognized by operators (Figures 7, 8, 9 and 10). This highlights how the network can overcome human observational limits, identifying active processes that were missing from the original ground truth. These findings indicate that the network has achieved a basic level of generalization capability, at least within the specific geomorphological domain of the study area. We must acknowledge that we carried out the test in a single study area and some leakage is possible even if all signals are different.

To assess the quality of the results and mitigate potential data leakage, we partitioned the dataset into an 80/10/10 split for training, validation, and testing, respectively. The training dynamics demonstrated stable convergence. The Total Loss curves for both training and validation sets exhibited a consistent downward trend, plateauing at a cost value of approximately 2.0 without diverging (See ancillary figure). Transient spikes observed in the validation loss (e.g., in the No-Object Loss around epoch 61) were rapidly mitigated by the network, highlighting the robustness of the optimization process. This behaviour confirms the absence of consistent overfitting, indicating that the model successfully learned underlying physical features rather than memorizing the training distribution. This is relevant because, unlike physical objects in optical imagery that possess sharp and unambiguous edges, landslide deformation patterns manifest as phase gradients with fuzzy boundaries. The transition from active deformation to stable ground is gradual and frequently obscured by phase noise. The model's ability to

maintain high localization precision despite this physical ambiguity highlights the effectiveness of the spatial feature extraction and the optimized anchor boxes in accurately delimiting the extent of the slope deformations.

5.2 The framework

Convolutional Neural Networks (CNNs), such as YOLO, are usually meant to ingest standard RGB images, with channels exhibiting high cross-correlation, effectively feeding the network structurally redundant information. Our strategy breaks inter-channel correlation to maximize the information gain and closely replicates the data integration process performed by human interpreters when interpreting deformation maps. Furthermore, unlike standard computer vision pipelines that compress inputs into an 8-bit optical format, our architecture is prepared to ingest and process the full original bit-depth of the input layers (e.g., 16-bit or floating-point values). This preserves the absolute radiometric integrity of the interferometric phase and coherence, preventing quantization errors and data loss. By providing orthogonal physical metrics, the network is forced to learn highly complex, non-linear feature representations within the first convolutional layer. While this heterogeneity increases the complexity of the initial optimization phase compared to standard optical datasets and it largely precludes the use of pre-trained layers, it provides a much richer feature space, enabling the architecture to detect subtle deformation patterns that would be entirely invisible or redundant in a traditional correlated multichannel setup.

To enhance the network's robustness and ensure it learns spatial and contextual deformation patterns rather than memorizing absolute channel values, we also introduced a radiometric perturbation step during training. This data augmentation technique applies random multiplicative scaling and additive shifting independently to the three input channels (mimicking variations in brightness, contrast, and phase unwrapping baselines). This forces the convolutional layers to rely on local gradients and structural coherence rather than absolute numerical thresholds, improving the model's generalization capabilities across different interferometric conditions. Given the peculiar statistical behaviour of the interferograms, this point should be further investigated in the future.

We designed and conducted this study as a methodological proof-of-concept rather than an attempt to develop a globally applicable, off-the-shelf landslide detection model. The primary focus of this research was to validate the feasibility and physical soundness of applying an object detection framework to InSAR data by engineering a novel, geomorphologically informed three-band input (comprising the interferogram, a sensitivity index, and the topographic PC1).

Because our core objective was to test this specific architectural adaptation, we neither intended nor pursued broad spatial generalization. Furthermore, developing a universally transferable deep learning model would inherently require an extensive training dataset representing diverse geomorphological conditions and SAR acquisition settings, which is currently unavailable. Consequently, the specific network weights obtained during this training phase are inevitably site-specific and tailored to the local interferometric signatures of the investigated area and data. The proposed multi-layered input architecture and the overall detection pipeline represent a scalable and replicable framework. This workflow can be readily applied and

fine-tuned in other mountainous regions as more comprehensive, localized annotated datasets become progressively available to the scientific community (e.g., Dini et al., 2025; Reyes-Carmona et al., 2026; Cusicanqui et al., 2026).

5.4 Implications for operational use

The proposed framework offers potential advantages for operational workflows. In a continuous monitoring scenario, every time a new SAR image is acquired, raw interferograms at various temporal baselines can be generated and processed by the network almost instantaneously. This rapid inference capability may support monitoring agencies and civil protection authorities in the quick screening of wide areas for newly activated or accelerating mass movements, drastically reducing the time required by the traditional visual inspections of massive datasets.

However, despite the high degree of automation and the rapid execution potentially offered by the network, we emphasize that the proposed framework is not fully autonomous and remains fundamentally expert-driven. Human expertise is currently irreplaceable in two critical phases of the operational workflow, namely the pre-selection of input and training data and the process-based interpretation of the results. The reliability of the network's predictions is strictly tied to the quality of the input. The process relies on the operator's ability to discard interferograms severely affected by atmospheric disturbances or widespread decorrelation, ensuring that only reliable signals are forwarded to the model.

The final assessment of the network's outputs still requires sound geomorphological judgment. Domain experts are essential to validate the detections and distinguish true, subtle kinematic signals—which may occasionally be flagged as false positives by rigid validation metrics—from complex phase artifacts. Consequently, the system is best intended as a highly efficient "expert-in-the-loop" tool. It automates the most time-consuming phase of spatial screening across multiple temporal baselines, while preserving the central role of the human interpreter for quality control and final geohazard evaluation.

6 Conclusions

We proposed an object detection framework based on a customized YOLO architecture to automatically detect and classify active mass movements from raw, wrapped Sentinel-1 interferograms. By integrating the phase signal with an InSAR sensitivity index and geomorphological metrics to reproduce the geomorphological process of the interpretation of the SAR signal carried out by the interpreters, the model achieved a mean Average Precision (mAP) of 0.88 and a global Recall of 0.93. These strong performance metrics demonstrate that AI-driven analysis of raw interferograms, constrained by sound geomorphological knowledge, can effectively identify complex deformation patterns across multiple spatial scales, capturing displacement signals that are often filtered out or missed by conventional multitemporal processing chains.

We designed and evaluated this network as a methodological proof-of-concept tailored to the specific geomorphological and interferometric signature of the Northern Apennines. The trained model is inherently a local product; the extracted features and specific network weights are highly site-specific and are not intended for direct generalization to different tectonic,

climatic, or geomorphological contexts. Applying this model to other regions would require extensive retraining on dedicated local datasets.

While further progress toward broader applicability will require larger, globally diverse training datasets and the integration of multi-frequency SAR observations, the proposed approach already constitutes a highly efficient tool at the regional scale. Operating as an expert-in-the-loop system, it significantly accelerates the spatial screening of slope instabilities, broadening the detectable range of displacement rates and effectively supporting the systematic update of landslide inventories.

Data availability

We used published or freely available datasets. We used the published geomorphological landslide inventory of Regione Emilia Romagna (RER, 2024), the Italian Landslide Inventory (IFFI, 2024) and GIS data available at https://geoportale.regione.emilia-romagna.it/). For DInSAR processing, we used Sentinel-1 data downloaded from the ASF Vertex portal and processed them using GMTSAR. The complete list of used SAR images and generated interferograms is provided in the Supplement with public access. To train and validate our deep learning model, we used the dataset published by Reyes-Carmona et al (2026), freely available on Zenodo (https://doi.org/10.5281/zenodo.17899662). The Python scripts used for the analysis are available from the first author upon reasonable request.

Author contributions

AMO, FA, AS and FB conceived the study. AMO designed the deep learning model. CR and AME performed the satellite DInSAR processing. FA, AS, CR and AME designed the labeling methodology. CR and AME performed the phase signal labeling supported by FA and AS. FB developed the ISM layer. AMO, FA and AS designed the validation methodology and interpreted the results. AM, AS, FA, FB and CR wrote the manuscript.

Competing interests

The authors declare that they have no conflicts of interest.

Acknowledgements

The authors thank Dr. Luca Dei Cas, Dr. Tazio Strozzi and Dr. Andrea Manconi for the fruitful discussions on the approaches to the automatic detection of landslides.

Financial support

The research was funded by the European Union - Next Generation EU, Mission 4, Component 2, CUP H53D23001660006 (PRIN22 Project "MIRAGE: Mass movement Investigation and prediction through geomorphology, Remote sensing and Artificial intelligence").

References

Agliardi, F., Scuderi, M. M., Fusi, N., and Collettini, C.: Slow-to-fast transition of giant creeping rockslides modulated by undrained loading in basal shear zones, Nat. Commun., 11, 1352. https://doi.org/10.1038/s41467-020-15093-3, 2020.

Agliardi, F. and Crippa, C.: Deep-Seated Gravitational Slope Deformations, in: Treatise on Geomorphology, Second Edition, Vol. 5, edited by: Shroder, J.J.F., Elsevier, Academic Press, London, UK, 183-199, https://dx.doi.org/10.1016/B978-0-12-818234-5.00182-6, 2022.

Agliardi, F., Mondini, A., Simoni, A., Reyes-Carmona, C., Mercurio, A. and Bovenga, F.: Automated detection and classification of active mass movements in SAR interferograms using a YOLO-based CNN, Geosciences and the Challenges of the 21st Century, Abstract Book of the SIMP-SGI Congress 2025, 993, https://doi.org/10.3301/ABSGI.2025.03, 2025.

Anantrasirichai, N., Biggs, J., Albino, F., Hill, P. and Bull, D.: Application of machine learning to classification of volcanic deformation in routinely generated InSAR data, J. Geophys. Res. Solid Earth, 123, 6592-6606, https://doi.org/10.1029/2018JB015911, 2018.

Ballantyne, C. K.: Paraglacial geomorphology, Quat. Sci. Rev., 21, 1935-2017, https://doi.org/10.1016/S0277-3791(02)00005-72002, 2002.

Bayer, B., Simoni, A., Mulas, M., Corsini, A. and Schmidt, D.: Deformation responses of slow moving landslides to seasonal rainfall in the Northern Apennines, measured by InSAR, Geomorphology, 308, 293-306, https://doi.org/10.1016/j.geomorph.2018.02.020, 2018.

Berti, M., Bertello, L., Bernardi, A.R., Caputo, G.: Back analysis of a large landslide in a flysch rock mass, Landslides, 14, 2041–2058, https:/doi.org/10.1007/s10346-017-0852-5, 2017.

Bekaert, D. P. S., Handwerger, A. L., Agram, P. and Kirschbaum, D. B.: InSAR-based detection method for mapping and monitoring slow-moving landslides in remote regions with steep and mountainous terrain: An application to Nepal, Remote Sens. Environ., 249, 111983, 2020.

Berardino, P., Fornaro, G., Lanari, R. and Sansosti, E.: A new algorithm for surface deformation monitoring based on small baseline differential SAR interferograms, IEEE Trans. Geosci. Remote Sens., 40, 2375-2383, 2003.

Bishop, C. M.: Pattern Recognition and Machine Learning, Springer, New York, NY, USA, 778 pp., ISBN 978-1-4939-3843-8, 2006.

Boccaletti, M., Corti, G., Martelli, L.: Recent and active tectonics of the external zone of the Northern Apennines (Italy). International Journal of Earth Sciences, 100, 1331–1348, 2011

Bovenga, F. and Piccolino, F.: InSAR Product Analysis (IPA): a QGIS tool for slope instability assessment based on SAR interferometry, EGU General Assembly 2025, Vienna, Austria, 27 April-2 May 2025, https://doi.org/10.5194/egusphere-egu25-17224, 2025.

Bovenga, F., Wasowski, J., Nitti, D. O., Nutricato, R. and Chiaradia, M. T.: Using COSMO/SkyMed X-band and ENVISAT C-band SAR interferometry for landslides analysis, Remote Sens. Environ., 119, 272-285, https://doi.org/10.1016/j.rse.2011.12.013, 2012.

Bovenga F, Mondini A, Simoni A, Reyes-Carmona C, Mercurio A, Agliardi F (2025). InSAR-based automated detection of active mass movements through YOLO CNN (Conference Presentation), SPIE Vol. 13670, Artificial Intelligence and Image and Signal Processing for Remote Sensing XXXI, Madrid, Spain, 28 October 2025, https://doi.org/10.1117/12.3069912, 2025.

Bralet, A., Trouvé, E., Chanussot, J., and Atto, A. M.: ISSLIDE: A new InSAR dataset for Slow SLIding area DEtection with machine learning. IEEE Geosci. Remote Sens. Lett., 21, 1-5, https://doi.org/10.1109/LGRS.2024.3365299, 2024.

Brengman, C. M. and Barnhart, W. D.: Identification of surface deformation in InSAR using machine learning, Geochem. Geophys. Geosyst., 22, e2020GC009204, https://doi.org/10.1029/2020GC009204, 2021.

Casagli, N., Intrieri, E., Tofani, V., Gigli, G. and Raspini, F.: Landslide detection, monitoring and prediction with remote-sensing techniques, Nat. Rev. Earth Environ., 4, 51-64, https://doi.org/10.1038/s43017-022-00373-x, 2023.

Capderou, M. (Ed.): Satellites, Orbits and Missions, Springer-Verlag, Paris, France, 544 pp., https://doi.org/10.1007/b139118, 2005.

Ciuffi, P., Bayer, B., Berti, M., Franceschini, S. and Simoni, A.: InSAR stacking to detect active landslides and investigate their relation to rainfalls in the Northern Apennines of Italy, Geomorphology, 457, 109242, https://doi.org/10.1016/j.geomorph.2024.109242, 2024.

Crippa, C., Valbuzzi, E., Frattini, P., Crosta, G. B., Spreafico, M. C. and Agliardi, F.: Semi-automated regional classification of the style of activity of slow rock-slope deformations using PS InSAR and SqueeSAR velocity data, Landslides, 18, 2445-2463, https://doi.org/10.1007/s10346-021-01654-0, 2021.

Cusicanqui, D., Laxroix, P., & Bodin, X. Moving areas Inventory based on InsSAR wrapped interferograms [Data set]. Zenodo. https://doi.org/10.5281/zenodo.18929451, 2026

Dasser, G., Maissen, A., Volpi, M., Aaron, J., Denzinger, F., Raetzo, H. and Manconi, A.: Towards automated identification of mass movements in spaceborne interferograms: Comparing expert mapping and deep learning approaches, Nat. Hazards Earth Syst. Sci. [preprint], https://doi.org/10.5194/egusphere-2026-375, 2026.

Dini, B., Manconi, A. and Loew, S.: Investigation of slope instabilities in NW Bhutan as derived from systematic DInSAR analyses, Eng. Geol., 259, 105111, https://doi.org/10.1016/j.enggeo.2019.04.008, 2019.

Dini, B., Lacroix, P., & Doin, M.-P. Wrapped interferograms and coherence Achoma landslide [Data set]. Zenodo. https://doi.org/10.5281/zenodo.17602759, 2026

Ferretti, A., Prati, C. and Rocca, F.: Permanent scatterers in SAR interferometry, IEEE Trans. Geosci. Remote Sens., 39, 8-20, https://doi.org/10.1109/36.898661, 2001.

Festa, D., Novellino, A., Hussain, E., Bateson, L., Casagli, N., Confuorto, P. et al.: Unsupervised detection of InSAR time series patterns based on PCA and K-means clustering, Int. J. Appl. Earth Obs. Geoinf., 118, 103276, https://doi.org/10.1016/j.jag.2023.103276, 2023.

Froude, M. J. and Petley, D. N.: Global fatal landslide occurrence from 2004 to 2016, Nat. Hazards Earth Syst. Sci., 18(8), 2161-2181, https://doi.org/10.5194/nhess-18-2161-2018, 2018.

Fruneau, B., Achache, J. and Delacourt, C.: Observation and modelling of the Saint-Etienne-de-Tinée landslide using SAR interferometry, Tectonophysics, 265, 181-190, https://doi.org/10.1016/S0040-1951(96)0004, 1996.

Fu, L., Zhang, Q., Wang, T., Li, W., Xu, Q. and Ge, D.: Detecting slow-moving landslides using InSAR phase-gradient stacking and deep-learning network, Front. Environ. Sci., 10, 963322, https://doi.org/10.3389/fenvs.2022.963322, 2022.

García-Davalillo, J. C., Herrera, G., Notti, D., Strozzi, T. and Álvarez-Fernández, I.: DInSAR analysis of ALOS PALSAR images for the assessment of very slow landslides: the Tena Valley case study, Landslides, 11, 225-246, https://doi.org/10.1007/s10346-012-0379-8, 2014.

Gessler, P., Pike, R., MacMillan, R. A., Hengl, T., & Reuter, H. I. (2009). The future of geomorphometry. Developments in Soil Science, 33, 637-652, 10.1016/S0166-2481(08)00028-7, 2009.

Goldstein, R. M. and Werner, C. L.: Radar interferogram filtering for geophysical applications, Geophys. Res. Lett., 25(21), 4035-4038, https://doi.org/10.1029/1998GL900033, 1998.

Graser, A., Sutton, T. and Bernasocchi, M.: The QGIS project: Spatial without compromise, Patterns, 6, 101265, https://doi.org/10.1016/j.patter.2025.101265, 2025.

Guzzetti, F., Mondini, A. C., Cardinali, M., Fiorucci, F., Santangelo, M. and Chang, K. T.: Landslide inventory maps: New tools for an old problem, Earth-Sci. Rev., 112, 42-66, https://doi.org/10.1016/j.earscirev.2012.02.001, 2012.

Handwerger, A. L., Huang, M. H., Fielding, E. J., Booth, A. M. and Bürgmann, R.: A shift from drought to extreme rainfall drives a stable landslide to catastrophic failure, Sci. Rep., 9, 1569, https://doi.org/10.1038/s41598-018-38300-0, 2019.

Handwerger, A. L., Roering, J. J. and Schmidt, D. A.: Controls on the seasonal deformation of slow-moving landslides, Earth Planet. Sci. Lett., 377, 239-247, https://doi.org/10.1016/j.epsl.2013.06.047, 2013.

Heaton, J.: Ian Goodfellow, Yoshua Bengio, and Aaron Courville: Deep Learning, Genet. Program. Evolvable Mach., 19, 305–307, https://doi.org/10.1007/s10710-017-9314-z, 2018.

Hengl, T., and Reuter, H.I. (eds.). Geomorphometry: Concepts, Software, Applications. Developments in Soil Science, 33, Elsevier, 772 pp, 2008.

Hotelling, H. Analysis of a complex of statistical variables into principal components. J. Educ. Psychol., 24, 417-441. http://dx.doi.org/10.1037/h0071325, 1933.

Hovius, N. and Stark, C. P.: Landslide-driven erosion and topographic evolution of active mountain belts, in: Landslides from Massive Rock Slope Failure, edited by: Evans, S. G., Mugnozza, G. S., Strom, A. and Hermanns, R. L., Springer, Dordrecht, The Netherlands, pp. 573-590, https://doi.org/10.1007/978-1-4020-4037-5_30, 2006.

ISPRA: *Inventario dei Fenomeni Franosi in Italia (IFFI)*. Dataset. Rome: Istituto Superiore per la Protezione e la Ricerca Ambientale. Available at: https://www.progettoiffi.isprambiente.it/ (Accessed: 2026).

Kalia, A. C.: Classification of landslide activity on a regional scale using Persistent Scatterer Interferometry at the Moselle Valley (Germany), Remote Sens., 10, 1880, https://doi.org/10.3390/rs10121880, 2018.

Korup, O., Densmore, A. L. and Schlunegger, F.: The role of landslides in mountain range evolution, Geomorphology, 120, 77-90, https://doi.org/10.1016/j.geomorph.2009.09.017, 2010.

IFFI Inventario dei Fenomeni Franosi in Italia (Landslide Inventory of Italy), Istituto Superiore per la Protezione e la Ricerca Ambientale (ISPRA). https://www.isprambiente.gov.it/it, 2024.

INSPIRE Geoportal, Catasto dei Rock Glacier in Alto Adige. https://inspire-geoportal.ec.europa.eu/srv/api/records/p_bz:Geology:RockGlaciers?language=all, 2010.

Lacroix, P., Handwerger, A. L. and Bièvre, G.: Life and death of slow-moving landslides, Nat. Rev. Earth Environ., 1(8), 404–419, https://doi.org/10.1038/s43017-020-0072-8, 2020.

Lloyd, S.: Least squares quantization in PCM, IEEE Trans. Inf. Theory, 28(2), 129–137, https://doi.org/10.1109/TIT.1982.1056489, 1982.

Manconi, A., Kourkouli, P., Caduff, R., Strozzi, T. and Loew, S.: Monitoring surface deformation over a failing rock slope with the ESA Sentinels: Insights from Moosfluh instability, Swiss Alps, Remote Sens., 10, 672, https://doi.org/10.3390/rs10050672, 2018.

Manconi, A.: How phase aliasing limits systematic space-borne DInSAR monitoring and failure forecast of Mackey and alpine landslides, Eng. Geol., 287, 106094, https://doi.org/10.1016/j.enggeo.2021.106094, 2021.

Mackey, B. H. and Roering, J. J.: Sediment yield, spatial characteristics, and the long-term evolution of active earthflows determined from airborne LiDAR and historical aerial photographs, Eel River, California, Geol. Soc. Am. Bull., 123, 1560-1576, https://doi.org/10.1130/B30306.1, 2011.

Medici, C., Novellino, A., Dashwood, C. and Bianchini, S.: Machine learning and clustering for supporting the identification of active landslides at national scale, Int. J. Appl. Earth Obs. Geoinf., 140, 104608, https://doi.org/10.1016/j.jag.2025.104608, 2025.

Mercurio, A., Bayer, B., Franceschini, S., Ciccarese, G., Bartola, M., Dal Seno, N., Rani, R., Zuccarini, A. and Simoni, A.: The potential of two-pass DInSAR to investigate the spatial and temporal evolution of a large landslide in the Northern

Apennines of Italy, EGU General Assembly 2025, Vienna, Austria, 27 April-2 May 2025, https://doi.org/10.5194/egusphere-egu25-11110, 2025.

Mondini, A. C., Guzzetti, F., Chang, K. T., Monserrat, O., Martha, T. R. and Manconi, A.: Landslide failures detection and mapping using Synthetic Aperture Radar: Past, present and future, Earth-Sci. Rev., 216, 103574, https://doi.org/10.1016/j.earscirev.2021.103574, 2021.

Mondini, A., Bovenga, F., Simoni, A., Reyes-Carmona, C., Mercurio, A. and Agliardi, F.: Automated detection of active mass movements in SAR interferograms using Deep Learning, EGU General Assembly 2025, Vienna, Austria, 27 April-2 May 2025, https://doi.org/10.5194/egusphere-egu25-16692, 2025.

Monti-Guarnieri, A. and Tebaldini, S.: On the Exploitation of Target Statistics for SAR Interferometry Applications, IEEE Trans. Geosci. Remote Sens., 46, 3436-3443, https://doi.org/10.1109/TGRS.2008.2001756, 2008.

Murray, K. D., Bekaert, D. P. and Lohman, R. B.: Tropospheric corrections for InSAR: Statistical assessments and applications to the Central United States and Mexico, Remote Sens. Environ., 232, https://doi.org/10.1016/j.rse.2019.111326, 2019.

Navarro, J. A., Tomás, R., Barra, A., Pagán, J. I., Reyes-Carmona, C., Solari, L., Vinielles, J. L., Falco, S. and Crosetto, M.: ADAtools: Automatic detection and classification of active deformation areas from PSI displacement maps, ISPRS Int. J. Geo-Inf., 9, https://doi.org/10.3390/ijgi9100584, 2020.

Notti, D., García-Davalillo, J. C., Herrera, G. and Mora, O.: Assessment of the performance of X-band satellite radar data for landslide mapping and monitoring: Upper Tena valley case study, Nat. Hazards Earth Syst. Sci., 10, 1865-1875, https://doi.org/10.5194/nhess-10-1865-2010, 2010.

Notti, D., Herrera, G., Bianchini, S., Meisina, C., García-Davalillo, J. C. and Zucca, F.: A methodology for improving landslide PSI data analysis, Int. J. Remote Sens., 35, 2186-2214, https://doi.org/10.1080/01431161.2014.889864, 2014.

Novellino, A., Cesarano, M., Cappelletti, P., Di Martire, D., Di Napoli, M., Ramondini, M. and Calcaterra, D.: Slow-moving landslide risk assessment combining Machine Learning and InSAR techniques, Catena, 203, 105317, https://doi.org/10.1016/j.catena.2021.105317, 2021.

QGIS Development Team: QGIS Geographic Information System, Open Source Geospatial Foundation Project, https://qgis.org, 2025.

Padilla, R., Netto, S. L. and da Silva, E. A. B.: A Survey on Performance Metrics for Object-Detection Algorithms, 2020 International Conference on Systems, Signals and Image Processing (IWSSIP), Ljubljana, Slovenia, 10-12 June 2026, 237-242, https://doi.org/10.1109/IWSSIP48289.2020.9145130, 2020.

Picotti, V., Pazzaglia, F.J.: A new active tectonic model for the construction of the Northern Apennines mountain front near Bologna (Italy). Journal of Geophysical Research 113, B08412. http://dx.doi.org/10.1029/2007JB005307, 2008

Pini, G.A.: Tectonosomes and olistostromes in the Argille Scagliose of Northern Apennines, Italy. Geol. Soc. Am. Spec. Pap., 335, 70 pp, 1999

Raspini, F., Bianchini, S., Ciampalini, A., Del Soldato, M., Montalti, R., Solari, L. and Casagli, N.: Persistent Scatterers continuous streaming for landslide monitoring and mapping: The case of the Tuscany region (Italy), Landslides, 16, 2033-2044, https://doi.org/10.1007/s10346-019-01249-w, 2019

Redmon, J., Divvala, S., Girshick, R. and Farhadi, A.: You only look once: Unified, real-time object detection. 2016 IEEE Conference on Computer Vision and Pattern Recognition (CVPR), Las Vegas, NV, USA, 779-788, 2016

R.E.R. Regione Emilia-Romagna - Servizio Geologico Sismico e dei Suoli: DTM (SGSS) – esteso – Modello Digitale del Terreno (cella di 10 m). Available at: https://geoportale.regione.emilia-romagna.it (Accessed: 2025), 2007

R.E.R. Regione Emilia-Romagna – Settore Difesa del Territorio: Inventario dei fenomeni franosi a scala 1:10000 della Regione Emilia-Romagna. Dataset. Available at: https://ambiente.regione.emilia-romagna.it/it/geologia/geologia/dissesto-idrogeologico/inventario-regionale-dei-fenomeni-franosi , 2025

Redmon, J. and Farhadi, A.: YOLOv3: An incremental improvement, arXiv [preprint], https://doi.org/10.48550/arXiv.1804.02767, 8 April 2018.

Reyes-Carmona, C., Mercurio, A., Mondini, A., Bovenga, F., Simoni, A. and Agliardi, F.: MIRAGE: a geomorphology-constrained dataset of DInSAR wrapped phase signals from active mass movements, Version v1, Zenodo [data set], https://doi.org/10.5281/zenodo.17899662, 2025

Reyes-Carmona, C., Mercurio, A., Mondini, A., Bovenga, F., Simoni, A. and Agliardi, F.: Dataset of DInSAR wrapped phase signals for AI-based automated detection and classification of mass movements, EarthArXiv [preprint], https://doi.org/10.31223/X5877Z, 26 March 2026.

Reyes-Carmona, C., Mercurio, A., Mondini, A., Bovenga, F., Simoni, A. and Agliardi, F.: Dataset of DInSAR wrapped phase signals for AI-based automated detection and classification of mass movements, manuscript under review in Sci. Data, 2026.

Rotter, P., and Muron, W.: Automatic detection of subsidence troughs in SAR interferograms based on convolutional neural networks. IEEE Geosci. Remote Sens. Lett, 18, 82-86, https://doi.org/10.1109/LGRS.2020.2966079, 2020.

Sandwell, D., Mellors, R., Tong, X., Wei, M., and Wessel, P.: GMTSAR: An InSAR Processing System Based on Generic Mapping Tools, Scripps Institution of Oceanography Technical Report, 2011.

Scotti, R., Brardinoni, F., Alberti, S., Frattini, P. and Crosta, G. B.: A regional inventory of rock glaciers and protalus ramparts in the central Italian Alps, Geomorphology, 186, 136-149, https://doi.org/10.1016/j.geomorph.2012.12.028, 2013.

Silva, B., Sousa, J. J., Lazecky, M. and Cunha, A.: Deformation fringes detection in SAR interferograms using deep learning, Procedia Comput. Sci., 196, 151-158, https://doi.org/10.1016/j.procs.2021.11.084, 2022.

Slaymaker, O.: Proglacial, periglacial or paraglacial?, in: Landscapes and Landforms of the Western Canadian Rockies, edited by: Slaymaker, O., Geological Society, London, Special Publications, 320, 71-84, https://doi.org/10.1144/SP320.10, 2009.

Simoni, A., Ponza, A., Picotti, V., Berti, M., Dinelli, E.: Earthflow sediment production and Holocene sediment record in a large Apennine catchment. Geomorphology 188, 42–53. https://doi.org /10.1016/j.geomorph.2012.12.006, 2013.

Springman, S. M., Arenson, L. U., Yamamoto, Y., Maurer, H., Kos, A., Buchli, T. and Derungs, G.: Multidisciplinary investigations on three rock glaciers in the Swiss Alps: Legacies and future perspectives, Geogr. Ann. A Phys. Geogr., 94, 215-243, https://doi.org/10.1111/j.1468-0459.2012.00464.x, 2012.

Squarzoni, G., Bayer, B., Franceschini, S. and Simoni, A.: Pre- and post-failure dynamics of landslides in the Northern Apennines revealed by space-borne synthetic aperture radar interferometry (InSAR), Geomorphology, 369, 107353, https://doi.org/10.1016/j.geomorph.2020.107353, 2020.

Strozzi, T., Jones, N., Agliardi, F., De Pedrini, A., Frey, O., Bernhard, P., Caduff, R., Ambrosi, C. and Manconi, A.: Monitoring the displacement of large alpine rock slope instabilities with L-band SAR interferometric techniques, Nat. Hazards Earth Syst. Sci. , https://doi.org/10.5194/nhess-26-2579-2026, 2026.

Touzi, R., Lopes, A., Bruniquel, J. and Vachon, P. W.: Coherence estimation for SAR imagery, IEEE Trans. Geosci. Remote Sens., 37, 135-149, https://doi.org/10.1109/36.739146, 1999.

Valloni, R. and Zuffa, G.G.: Provenance changes for arenaceous formations of the northern Apennines, Italy. Geological Society of America Bulletin, 95(9), 1035-1039, 1984

Van Natijne, A. L., Bogaard, T. A., Van Leijen, T. A., Hanssen, R. F. and Lindenbergh, R. C.: World-wide InSAR sensitivity index for landslide deformation tracking, Int. J. Appl. Earth Obs. Geoinf., 111, 102829, https://doi.org/10.1016/j.jag.2022.102829, 2022.

Wasowski, J. and Bovenga, F.: Investigating landslides and unstable slopes with satellite Multi Temporal Interferometry: Current issues and future perspectives, Eng. Geol., 174, 103-138, https://doi.org/10.1016/j.enggeo.2014.03.003, 2014.

Wasowski, J. and Bovenga, F.: Remote Sensing of Landslide Motion with Emphasis on Satellite Multitemporal Interferometry Applications: An Overview, in: Landslide Hazards, Risks and Disasters (Second Edition), edited by: Davies, T., Rosser, N. and Shroder, J. F., Elsevier Inc., Amsterdam, The Netherlands, 365-438, https://doi.org/10.1016/B978-0-12-818464-6.00006-8, 2022.

Zebker, H. A. and Villasenor, J.: Decorrelation in interferometric radar echoes, IEEE Trans. Geosci. Remote Sens., 30, 950-959, 1992.

Zhang, R., Zhu, W., Fan, B., He, Q., Zhan, J., Wang, C. and Zhang, B.: MB-Net: A network for accurately identifying creeping landslides from wrapped interferograms, Int. J. Appl. Earth Obs. Geoinf., 135, 104300, https://doi.org/10.1016/j.jag.2024.104300, 2024.

Zhang, C., Luo, J. and Li, Z.: An Automatic Detection Method of Slow-Moving Landslides Using an Improved Faster R-CNN Model Based on InSAR Deformation Rates, Remote Sens., 17, 3243, https://doi.org/10.3390/rs17183243, 2025.

Zhou, C., Ye, M., Xia, Z., Wang, W., Luo, C. and Muller, J. P.: An interpretable attention-based deep learning method for landslide prediction based on multi-temporal InSAR time series: A case study of Xinpu landslide in the TGRA, Remote Sens. Environ., 318, 114580, https://doi.org/10.1016/j.rse.2024.114580, 2025.

Zhu, X. X., Montazeri, S., Ali, M., Hua, Y., Wang, Y., Mou, L., Shi, Y., Xu, F. and Bamler, R.: Deep learning meets SAR: Concepts, models, pitfalls, and perspectives, IEEE Geosci. Remote Sens. Mag., 9, 143-172, https://doi.org/10.1109/MGRS.2020.3046356, 2021.

885 **Supplementary material**

date (from_to)	temporal baseline (days)	perpendicular baseline (m)	orbit
20161130_20161218	18	14.7	DESC
20161201_20161213	12	40.0911	ASC
20161201_20161225	24	16.33	ASC
20161213_20161225	12	5.5	ASC
20161213_20161231	18	13.5	ASC
20161225_20161231	6	12.73	ASC
20170211_20170307	24	24.46	ASC
20170301_20170307	6	9.76	ASC
20180401_20180407	6	20.44	ASC
20180401_20180413	12	22.37	ASC
20190213_20190219	6	4.54	ASC
20191128_20191210	12	18.06	ASC
20191204_20191210	6	8.85	ASC
20191227_20200108	12	4.73	DESC
20191227_20200114	18	73.39	DESC
20191228_20200121	24	6.44	ASC
20200102_20200108	6	2.44	DESC
20200102_20200114	12	2.83	DESC
20200109_20200121	12	10.89	ASC
20200109_20200127	18	18.17	ASC
20200115_20200127	12	15.43	ASC
20200121_20200127	6	3.42	ASC
20200207_20200213	6	8.79	DESC
20200214_20200220	6	25.44	DESC
20200214_20200303	18	43.88	ASC
20200214_20200315	30	48.03	ASC
20200219_20200314	24	21.41	DESC
20200308_20200314	6	12.93	DESC
20200315_20200402	18	20.8	ASC
20210103_20210121	12	29.96	ASC
20210127_20210202	6	9.81	ASC
20210127_20210208	12	10.23	ASC

20210201_20210207	6	15.58	DESC
20210202_20210208	6	11.78	ASC
20210202_20210220	18	28.55	ASC
20210225_20210303	6	88.92	DESC
20210303_20210315	12	70.78	DESC
20210303_20210321	18	47.44	DESC
20210304_20210310	6	28.27	ASC
20210304_20210316	12	11.79	ASC
20210304_20210322	18	17.49	ASC
20210310_20210322	12	13.61	ASC
20210322_20210328	6	4.93	DESC
20210327_20210402	6	19.73	DESC
20211222_20220103	12	12.01	DESC
20220208_20220220	12	19.12	DESC
20220209_20220305	24	27.94	ASC
20220316_20220328	12	13.76	DESC
20221206_20221218	12	23.85	ASC
20230312_20230324	12	23.47	ASC
20240306_20240318	12	45.36	ASC
20250204_20250216	12	30.09	DESC
20250204_20250228	24	20.1	DESC
20250216_20250228	12	32.09	DESC
20250217_20250313	24	5.12	ASC
20250324_20250405	12	59.51	DESC

Table S1. List of interferograms selected for expert interpretation and subsequent model training, testing and validation.

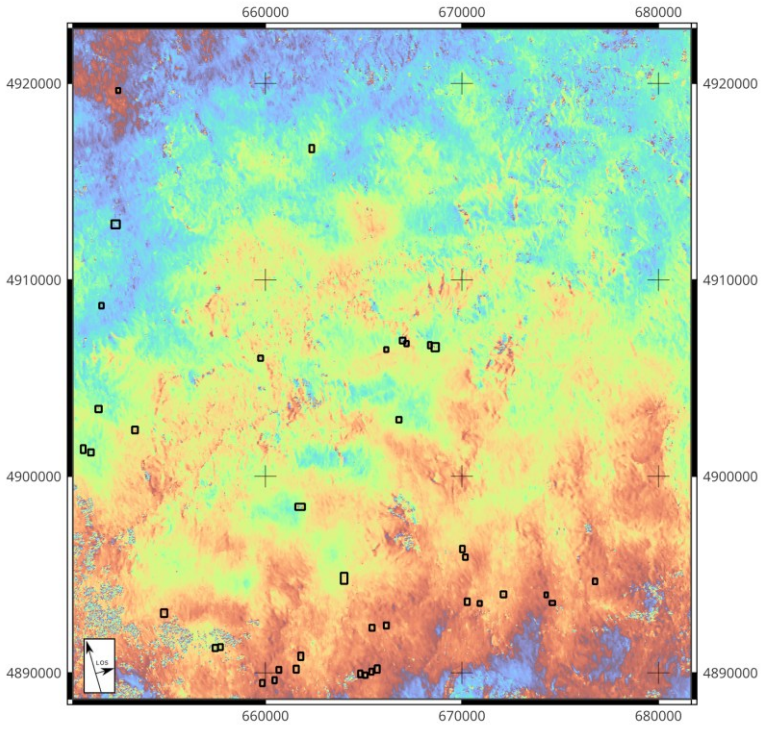

Fig. S1. Example wrapped interferogram selected for expert interpretation with associated annotations (Asc 20161213_20161225).

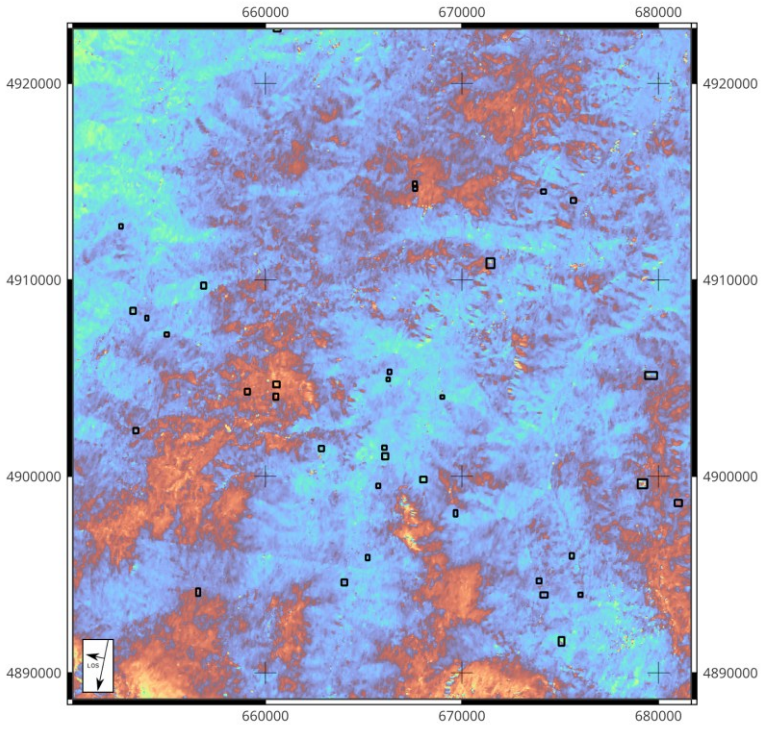

Fig. S1. Example wrapped interferogram selected for expert interpretation with associated annotations (Desc 20191227_20200114).

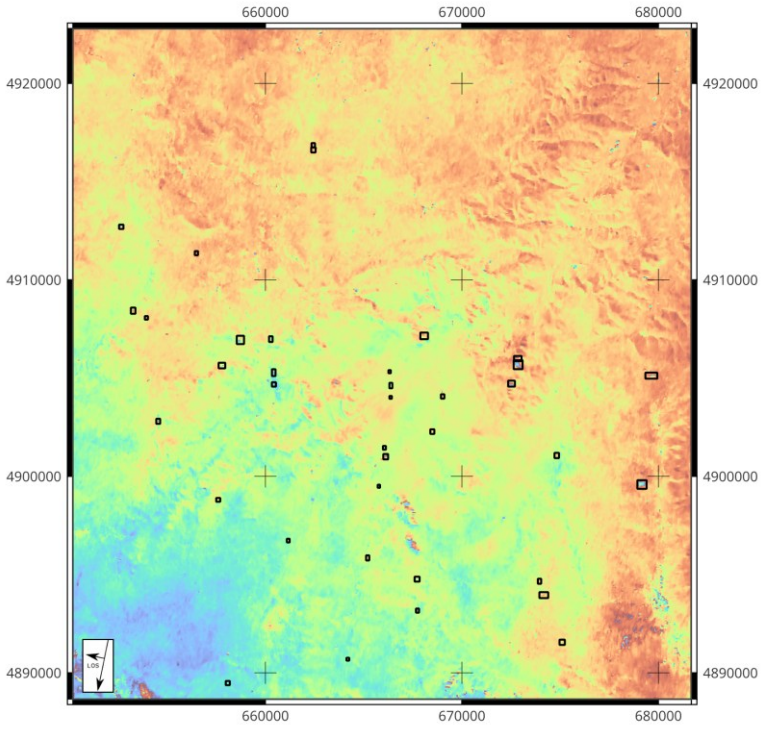

Fig. S1. Example wrapped interferogram selected for expert interpretation with associated annotations (Desc 20200102_20200114).

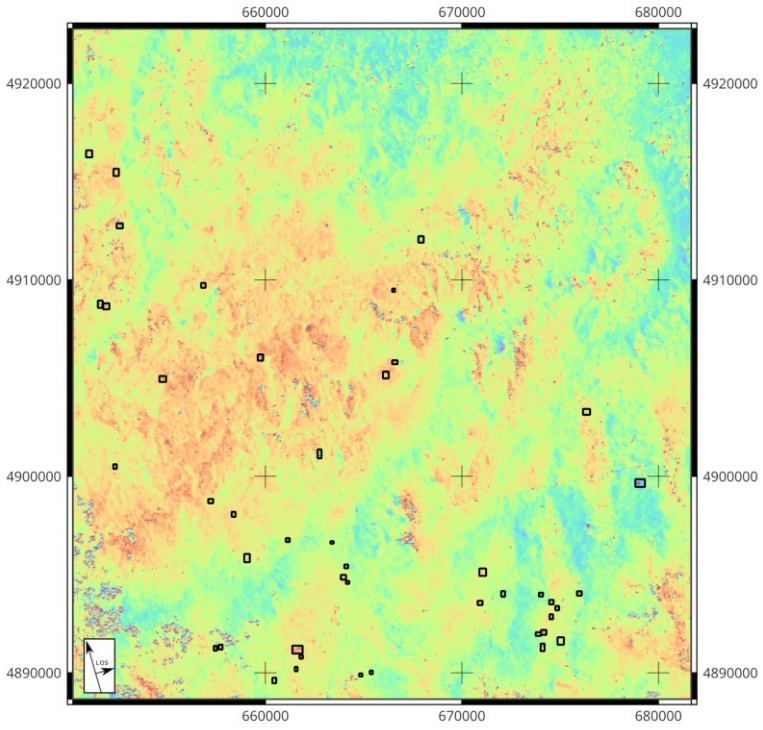

Fig. S1. Example wrapped interferogram selected for expert interpretation with associated annotations (Desc 20200315_20200402).

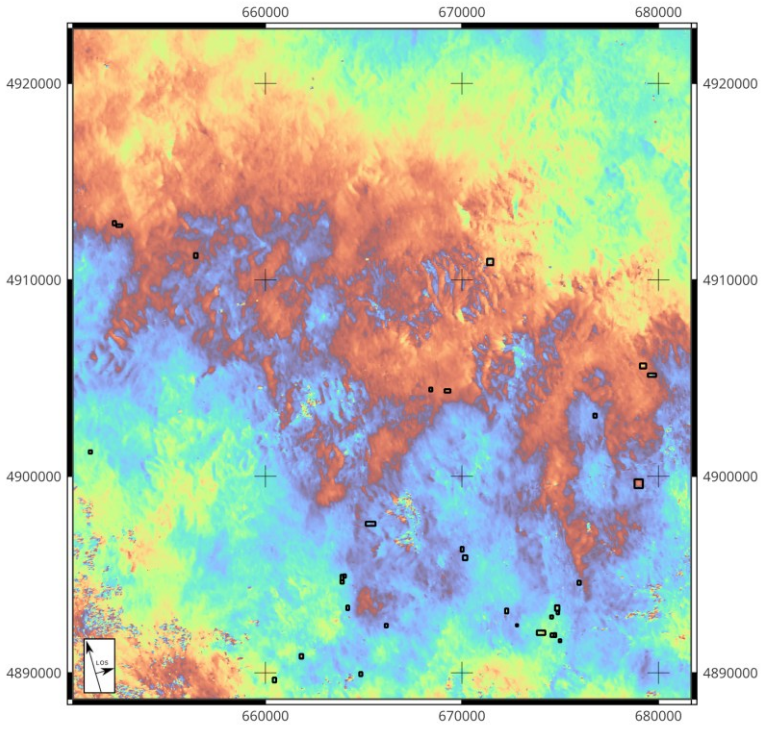

Fig. S1. Example wrapped interferogram selected for expert interpretation with associated annotations (Asc 20210304_20210310).

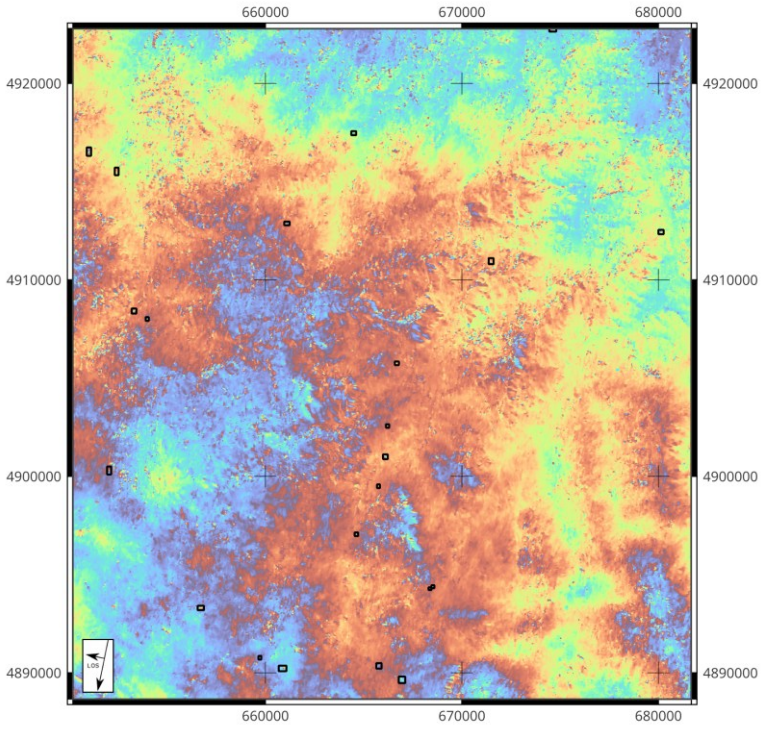

Fig. S1. Example wrapped interferogram selected for expert interpretation with associated annotations (Desc 20250324_20250405).